$B_s \to K\ell\nu$ decay from lattice QCD

A. Bazavov,[1] C. Bernard,[2] C. DeTar,[3] Daping Du,[4] A. X. El-Khadra,[5,6] E. D. Freeland,[7] E. Gámiz,[8] Z. Gelzer,[5] Steven Gottlieb,[9] U. M. Heller,[10] A. S. Kronfeld,[6,11] J. Laiho,[4] Yuzhi Liu,[9] P. B. Mackenzie,[6] Y. Meurice,[12] E. T. Neil,[13,14] J. N. Simone,[6] R. Sugar,[15] D. Toussaint,[16] R. S. Van de Water,[6] and Ran Zhou[6]

(Fermilab Lattice and MILC Collaborations)

[1]*Department of Computational Mathematics, Science and Engineering, and Department of Physics and Astronomy, Michigan State University, East Lansing, Michigan 48824, USA*
[2]*Department of Physics, Washington University, St. Louis, Missouri 63130, USA*
[3]*Department of Physics and Astronomy, University of Utah, Salt Lake City, Utah 84112, USA*
[4]*Department of Physics, Syracuse University, Syracuse, New York 13244, USA*
[5]*Department of Physics, University of Illinois, Urbana, Illinois 61801, USA*
[6]*Fermi National Accelerator Laboratory, Batavia, Illinois 60510, USA*
[7]*Liberal Arts Department, School of the Art Institute of Chicago, Chicago, Illinois, USA*
[8]*CAFPE and Departamento de Fisica Teórica y del Cosmos, Universidad de Granada, E-18071 Granada, Spain*
[9]*Department of Physics, Indiana University, Bloomington, Indiana 47405, USA*
[10]*American Physical Society, Ridge, New York 11961, USA*
[11]*Institute for Advanced Study, Technische Universität München, 85748 Garching, Germany*
[12]*Department of Physics and Astronomy, University of Iowa, Iowa City, Iowa, USA*
[13]*Department of Physics, University of Colorado, Boulder, Colorado 80309, USA*
[14]*RIKEN-BNL Research Center, Brookhaven National Laboratory, Upton, New York 11973, USA*
[15]*Department of Physics, University of California, Santa Barbara, California 93106, USA*
[16]*Physics Department, University of Arizona, Tucson, Arizona 85721, USA*

(Received 21 January 2019; published 1 August 2019)

We use lattice QCD to calculate the form factors $f_+(q^2)$ and $f_0(q^2)$ for the semileptonic decay $B_s \to K\ell\nu$. Our calculation uses six MILC asqtad $2+1$ flavor gauge-field ensembles with three lattice spacings. At the smallest and largest lattice spacing the light-quark sea mass is set to $1/10$ the strange-quark mass. At the intermediate lattice spacing, we use four values for the light-quark sea mass ranging from $1/5$ to $1/20$ of the strange-quark mass. We use the asqtad improved staggered action for the light valence quarks, and the clover action with the Fermilab interpolation for the heavy valence bottom quark. We use SU(2) hard-kaon heavy-meson rooted staggered chiral perturbation theory to take the chiral-continuum limit. A functional z expansion is used to extend the form factors to the full kinematic range. We present predictions for the differential decay rate for both $B_s \to K\mu\nu$ and $B_s \to K\tau\nu$. We also present results for the forward-backward asymmetry, the lepton polarization asymmetry, ratios of the scalar and vector form factors for the decays $B_s \to K\ell\nu$ and $B_s \to D_s\ell\nu$. Our results, together with future experimental measurements, can be used to determine the magnitude of the Cabibbo-Kobayashi-Maskawa matrix element $|V_{ub}|$.

DOI: 10.1103/PhysRevD.100.034501

I. INTRODUCTION

Semileptonic decays of hadrons can be used to determine elements of the Cabibbo-Kobayashi-Maskawa (CKM) matrix. However, since the quarks that participate in the underlying electroweak transition are constituents of bound states, it is necessary to understand the effects of the strong interactions on the decay. These effects are encapsulated in form factors for hadronic matrix elements of the weak currents that govern the decay. Lattice QCD has allowed us to calculate the form factors with increasing precision, making possible stringent tests of the Standard Model and the CKM paradigm. Should there be a violation of unitarity of the CKM matrix, or should two decay processes that depend

on the same CKM matrix element imply different values for that CKM matrix element, we would have evidence for physics beyond the Standard Model. The decay studied here, $B_s \to K\ell\nu$ depends on the same matrix element V_{ub} as the decay $B \to \pi\ell\nu$. Indeed, the only difference between the two decay processes is that the light spectator up (u) or down (d) quark in the latter process is replaced by a strange (s) quark in the case at hand. Since in lattice QCD, strange quarks generally yield smaller statistical errors and are easier to deal with computationally, a lattice calculation of the form factors for $B_s \to K\ell\nu$ decay can enable a precise $|V_{ub}|$ determination. This, in turn, can provide a useful test of $|V_{ub}|$ determinations from the exclusive $B \to \pi\ell\nu$ and $\Lambda_b \to p\ell\nu$ processes, and, if consistent, a reduced error on $|V_{ub}|$ (exclusive) after combination.

On the experimental side, however, while *BABAR* [1,2] and Belle [3,4] have published precise measurements of the differential decay rate for $B \to \pi\ell\nu$, no such measurements exist yet for $B_s \to K\ell\nu$. The branching fraction of the former decay is $(7.80 \pm 0.27) \times 10^{-5}$ [5], as it is Cabibbo suppressed compared to final states with charm. As *BABAR* and Belle observed many more $B\bar{B}$ than $B_s\bar{B}_s$ events, it is not surprising that experimental measurements of the latter decay have not yet been reported. In contrast, the LHCb experiment at the CERN LHC collider observes decays of all b-flavored hadrons, including B_s mesons. They are expected to publish the results of their ongoing $B_s \to K\ell\nu$ decay study within the coming year [6]. The Belle II experiment [7], where the e^+e^- collisions provide a cleaner environment than at the LHC, also expects to study this decay. The current plans are that Belle II will collect about 50 ab^{-1} at the $\Upsilon(4S)$ resonance (which decays predominantly into B-meson pairs), and 5 ab^{-1} at the $\Upsilon(5S)$, a rich source of B_s-meson pairs [7]. Thus, we do not expect the experimental accuracy for Belle II's future measurement of $B_s \to K\ell\nu$ decay rates to rival that of their expected results for $B \to \pi\ell\nu$, but we do expect this decay to be studied by Belle II.

This work is part of a broad study of flavor physics by the Fermilab Lattice and MILC Collaborations to determine a number of CKM matrix elements from semileptonic K [8], $D_{(s)}$ [9], and $B_{(s)}$ [10–19] decays using the asqtad $2+1$ flavor ensembles generated by the MILC Collaboration [20–22]. These studies are currently being extended [23–27] to use HISQ $2+1+1$ flavor ensembles [28,29]. These newer ensembles include ones with physical-mass Goldstone pions at several lattice spacings that significantly improve our control of the chiral limit. In order to provide a systematic mode by mode comparison of results obtained with the two sets of configurations, it is important to complete this analysis of $B_s \to K\ell\nu$.

The techniques used here are very similar to those employed in Ref. [16], where the functional z expansion was introduced. However, in this work, we use a subset of six MILC ensembles covering a range of lattice spacing a between approximately 0.12 and 0.06 fm. Prior work used 12 ensembles including one with $a \approx 0.045$ fm.

The decay $B_s \to K\ell\nu$ has been studied by three other lattice-QCD groups, the HPQCD Collaboration [30], the RBC and UKQCD Collaborations [31], and the ALPHA Collaboration [32], each choosing different actions for the b-quark and for the light sea and valence quarks. Other previous calculations of the $B_s \to K\ell\nu$ decay form factors are based on the relativistic quark model [33], light-cone sum rules [34,35], and next-to-leading-order (NLO) perturbative QCD [36]. In Sec. VI C, we compare our results with the prior results. Preliminary reports on this study can be found in Refs. [37,38], where the vector current renormalization factors were still multiplied by a blinding factor. This factor was disclosed only after the analysis was finalized.

The rest of this paper is organized as follows. In Sec. II, we define the continuum decay form factors and the hadronic matrix elements needed to calculate them. In Sec. III, we introduce the lattice QCD operators and the form factors most convenient to calculate on the lattice. We detail how to calculate the needed lattice matrix elements and enumerate the MILC asqtad $2+1$ flavor ensembles we have used. Section IV discusses our analysis of the two- and three-point functions needed to construct the lattice form factors. We also explain how we take the chiral-continuum limit. Section V contains our analysis of systematic errors in the range of momentum transfer accessible in our calculation. To construct the continuum form factors over the entire range of momentum transfer, we present the functional z expansion in Sec. VI. We then apply it to obtain our final results for the form factors. Section VII presents some of the phenomenological implications of the results. Appendix A contains details of our application of SU(2) chiral perturbation theory to perform the chiral extrapolation in Sec. IV. Appendix B details how we construct the continuum form factors in Sec. VI B. Appendix C contains the binned differential decay rates, as well as the full correlation matrices.

II. MATRIX ELEMENTS AND FORM FACTORS

To lowest order in the weak coupling constant, the semileptonic $B_s \to K\ell\nu$ decay can be described via the Feynman diagram shown in Fig. 1. The relevant hadronic matrix element can be written as

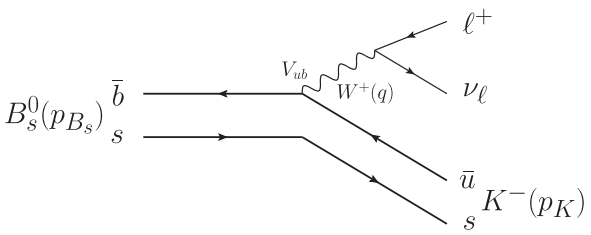

FIG. 1. Lowest order Standard Model Feynman diagram shown here for example of semileptonic $B_s^0 \to K^-\ell^+\nu_\ell$ decay.

$$\langle K(p_K)|\mathcal{V}^\mu|B_s(p_{B_s})\rangle = \left(p_K^\mu + p_{B_s}^\mu - q^\mu \frac{M_{B_s}^2 - M_K^2}{q^2}\right) f_+(q^2) + q^\mu \frac{M_{B_s}^2 - M_K^2}{q^2} f_0(q^2), \tag{2.1}$$

where $\mathcal{V}^\mu \equiv \bar{u}\gamma^\mu b$ is the vector current, $p_{B_s}^\mu$ and p_K^μ are the B_s and K four-momenta, respectively, M_{B_s} and M_K are the corresponding meson masses, $q^\mu = p_{B_s}^\mu - p_K^\mu$ is the momentum transferred to the lepton pair, and $f_+(q^2)$ and $f_0(q^2)$ are the vector and scalar form factors corresponding to the exchange of 1^- and 0^+ particles. These two form factors are subject to a kinematic constraint:

$$f_+(0) = f_0(0), \tag{2.2}$$

which eliminates the spurious pole at $q^2 = 0$ in Eq. (2.1). The tensor form factor f_T parametrizes the hadronic matrix element of the tensor current $T^{\mu\nu} = i\bar{u}\sigma^{\mu\nu}b$. Since it does not contribute to the Standard Model decay rate, we do not include it in this calculation.

In the Standard Model, the angular-dependent differential decay rate for the $B_s \to K\ell\nu$ can be written as

$$\frac{d^2\Gamma}{dq^2 d\cos\theta_\ell} = \frac{G_F^2|V_{ub}|^2}{128\pi^3 M_{B_s}^2}\left(1 - \frac{m_\ell^2}{q^2}\right)^2 |\mathrm{p}_K| \left[4M_{B_s}^2|\mathrm{p}_K|^2\left(\sin^2\theta_\ell + \frac{m_\ell^2}{q^2}\cos^2\theta_\ell\right)\left|f_+(q^2)\right|^2 + \frac{4m_\ell^2}{q^2}(M_{B_s}^2 - M_K^2)M_{B_s}|\mathrm{p}_K|\cos\theta_\ell \mathrm{Re}[f_+(q^2)f_0^*(q^2)] + \frac{m_\ell^2}{q^2}(M_{B_s}^2 - M_K^2)^2|f_0(q^2)|^2\right] \tag{2.3}$$

in the B_s meson rest frame. Here G_F is the Fermi constant, V_{ub} is an element of the CKM matrix, m_ℓ is the lepton mass, and θ_ℓ is the angle between the final charged lepton and the B_s meson momenta in the rest frame of the final state leptons. Thus, to determine $|V_{ub}|$ from a measurement of the differential decay rate, it is necessary to compute the form factor $f_+(q^2)$. If the charged lepton is the τ, however, the lepton mass cannot be neglected and $f_0(q^2)$ is also necessary.

III. LATTICE-QCD CALCULATION

In this section, we present the ingredients of our lattice-QCD calculation. The definitions of form factors and correlation functions are given in Sec. III A. The lattice actions and simulation parameters are described in Sec. III B. The lattice interpolating operators, currents, and correlation functions are presented in Sec. III C.

A. Definitions

For lattice calculations and Heavy Quark Effective Theory (HQET), it is convenient to work in the B_s rest frame and introduce the B_s four-velocity

$$v^\mu = p_{B_s}^\mu / M_{B_s}. \tag{3.1}$$

The square of the lepton momentum transfer q^2 can then be expressed as

$$q^2 = (p_{B_s}^\mu - p_K^\mu)^2 = M_{B_s}^2 + M_K^2 - 2M_{B_s}E_K, \tag{3.2}$$

where $E_K = p_K \cdot v$ is the kaon energy. Defining

$$p_\perp^\mu \equiv p_K^\mu - (p_K \cdot v)v^\mu \tag{3.3}$$

as the projection of the kaon momentum in the direction perpendicular to v^μ and using Eq. (3.2), one can rewrite the matrix element Eq. (2.1) in terms of the form factors $f_\parallel(E_K)$ and $f_\perp(E_K)$ as

$$\langle K(p_K)|\mathcal{V}^\mu|B_s(p_{B_s})\rangle = \sqrt{2M_{B_s}}[v^\mu f_\parallel(E_K) + p_\perp^\mu f_\perp(E_K)]. \tag{3.4}$$

The relations to the original form factors f_+ and f_0 are given by

$$f_+(q^2) = \frac{1}{\sqrt{2M_{B_s}}}[f_\parallel(E_K) + (M_{B_s} - E_K)f_\perp(E_K)], \tag{3.5a}$$

$$f_0(q^2) = \frac{\sqrt{2M_{B_s}}}{M_{B_s}^2 - M_K^2}[(M_{B_s} - E_K)f_\parallel(E_K) + (E_K^2 - M_K^2)f_\perp(E_K)]. \tag{3.5b}$$

The kinematic constraint, Eq. (2.2), is automatically satisfied in Eq. (3.5).

In the B_s rest frame, which we use throughout the lattice-QCD calculation, the form factors $f_\parallel$ and $f_\perp$ are related to the temporal and spatial components of the matrix element of the vector current $\mathcal{V}^\mu$ via

$$f_\parallel(E_K) = \frac{\langle K|\mathcal{V}^0|B_s\rangle}{\sqrt{2M_{B_s}}}, \tag{3.6a}$$

$$f_\perp(E_K) = \frac{\langle K|\mathcal{V}^i|B_s\rangle}{\sqrt{2M_{B_s}}}\frac{1}{p_K^i}. \tag{3.6b}$$

TABLE I. Parameters used for generating the lattice QCD gauge fields. The columns from left to right are approximate lattice spacing a in fm, the lattice dimensions in lattice units $N_s^3 \times N_t$, the sea-quark mass ratios am_l'/am_h', the gauge coupling β, the tadpole improvement factor u_0, the number of gauge-field configurations $N_{\rm conf}$, and the pion mass times the box linear spatial size $M_\pi L$ ($L = N_s a$). The gauge-field configurations can be downloaded using the DOI links provided in Refs. [49–58].

≈a (fm)	$N_s^3 \times N_t$	am_l'/am_h'	β	u_0	$N_{\rm conf}$	$M_\pi L$
0.12 [49]	$24^3 \times 64$	0.0050/0.050	6.76	0.8678	2099	3.8
0.09 [50–52]	$28^3 \times 96$	0.0062/0.031	7.09	0.8782	1931	4.1
0.09 [53]	$32^3 \times 96$	0.00465/0.031	7.085	0.8781	1015	4.1
0.09 [54,55]	$40^3 \times 96$	0.0031/0.031	7.08	0.8779	1015	4.2
0.09 [56]	$64^3 \times 96$	0.00155/0.031	7.075	0.877805	791	4.8
0.06 [57,58]	$64^3 \times 144$	0.0018/0.018	7.46	0.88764	827	4.3

Note that there is no summation over the superscript i in Eq. (3.6b). The continuum-QCD current is related to the lattice current operator V^μ by a multiplicative renormalization factor, i.e.,

$$\mathcal{V}^\mu(x) = Z_{V_\mu} V^\mu(x). \tag{3.7}$$

The lattice current V^μ is defined in Sec. III C, below. We use a mostly nonperturbative method to compute Z_{V_μ}. The details are explained in Sec. III C.

The desired matrix elements (and hence form factors) can be calculated from suitably defined two- and three-point correlation functions:

$$C_2^{B_s}(t;\boldsymbol{p}_{B_s}=0) = \sum_{\boldsymbol{x}} \langle \mathcal{O}_{B_s}(0,\boldsymbol{0}) \mathcal{O}_{B_s}^\dagger(t,\boldsymbol{x})\rangle, \tag{3.8a}$$

$$C_2^{K}(t;\boldsymbol{p}_K) = \sum_{\boldsymbol{x}} \langle \mathcal{O}_{K}(0,\boldsymbol{0}) \mathcal{O}_{K}^\dagger(t,\boldsymbol{x})\rangle e^{i\boldsymbol{p}_K\cdot\boldsymbol{x}}, \tag{3.8b}$$

$$C_{3,\mu}^{B_s\to K}(t,T;\boldsymbol{p}_K) = \sum_{\boldsymbol{x},\boldsymbol{y}} \langle \mathcal{O}_{K}(0,\boldsymbol{0}) V^\mu(t,\boldsymbol{y}) \mathcal{O}_{B_s}^\dagger(T,\boldsymbol{x})\rangle e^{i\boldsymbol{p}_K\cdot\boldsymbol{y}}, \tag{3.8c}$$

where $\mathcal{O}_{B_s}$ and $\mathcal{O}_K$ are lattice interpolating operators, which are defined in Sec. III C, below. Further, $\boldsymbol{p}_K$ is the kaon spatial momentum, whose components in a finite volume are integer multiples of $2\pi/N_s$, where N_s is the lattice spatial dimension in lattice units.

The basic procedure for calculating the continuum form factors f_+ and f_0 in Eq. (2.1) in lattice QCD is the following:

(1) For each ensemble:
   (i) Determine the lattice B_s meson masses, kaon masses, and energies from the lattice two-point correlation functions.
   (ii) Determine the lattice form factors $f_\parallel^{\rm lat}$ and $f_\perp^{\rm lat}$ at several discrete kaon momenta $\boldsymbol{p}_K$ from the two- and three-point correlation functions.
   (iii) Obtain the renormalized form factors by matching the lattice current to the continuum as in Eq. (3.7).
(2) Use chiral perturbation theory together with Symanzik effective theory to perform a combined chiral-continuum fit to the renormalized form factors and extrapolate them to the physical quark masses and continuum (zero lattice spacing) limits. This yields the continuum form factors $f_\parallel$ and $f_\perp$ as functions of the kaon recoil energy E_K in the interval covered by the simulation, roughly $0.5\ {\rm GeV} \lesssim E_K \lesssim 1\ {\rm GeV}$.
(3) Construct the continuum form factors f_+ and f_0 from $f_\parallel$ and $f_\perp$ via Eq. (3.5) and employ a z expansion to parametrize their shapes and to extrapolate them from the low-recoil range to the entire kinematically allowed region, which extends at high recoil to $q^2 = 0$.

B. Actions and parameters

We use lattice gauge configurations with $N_f = 2+1$ flavors generated by the MILC Collaboration [20–22]. These configurations include two degenerate dynamical light quarks, acting as u and d quarks, and one heavier, s, quark. The gluon fields are simulated with the one-loop improved Lüscher-Weisz action [39]. The a^2 tadpole-improved staggered action (asqtad) [40–46] is used for generating dynamical light quarks (u, d, and s). Reference [22] is a review of simulations and formalism of improved staggered quarks.

The asqtad fermion action is also used for the valence u, d, and s quarks. The heavy valence bottom (b) quarks use the Sheikholeslami-Wohlert (SW) Wilson-clover action [47] with the Fermilab interpretation [48].

Some of the parameters used to generate the configurations are listed in Table I. Six ensembles with three different lattice spacings, $a \approx 0.12$, 0.09, and 0.06 fm, are used. For each lattice spacing, we have dynamical sea quarks with light-to-strange quark mass ratio

TABLE II. Parameters used for generating the valence quarks. The approximate lattice spacing a and lattice dimensions $N_s^3 \times N_t$ in the first two columns identify the ensemble. The light valence quarks m_l are degenerate with the sea quarks m'_l. The valence s quarks m_h are better tuned than the sea s quarks m'_h. The parameters $c_{\rm sw}$ and κ'_b are used in the SW action for b quarks. The rotation parameter d_1 is used in the current.

≈a (fm)	$N_s^3 \times N_t$	am_l/am_h	$c_{\rm sw}$	κ'_b	d_1
0.12	$24^3 \times 64$	0.0050/0.0336	1.53	0.0901	0.09332
0.09	$28^3 \times 96$	0.0062/0.0247	1.476	0.0979	0.096765
0.09	$32^3 \times 96$	0.00465/0.0247	1.477	0.0977	0.096708
0.09	$40^3 \times 96$	0.0031/0.0247	1.478	0.0976	0.096688
0.09	$64^3 \times 96$	0.00155/0.0247	1.478	0.0976	0.0967
0.06	$64^3 \times 144$	0.0018/0.0177	1.4298	0.1052	0.0963

$m'_l/m'_h = 0.1$.[1] For the intermediate lattice spacing $a \approx 0.09$ fm, we have three additional values of $m'_l/m'_h = 0.05$, 0.15, and 0.2 to provide results for the chiral extrapolation. The subset of ensembles used for the analysis is based on experience from previous semileptonic form factor analyses [16,18]. The tadpole factor u_0 appearing in the one-loop improved Lüscher-Weisz gauge action and in the asqtad fermion action are determined from the fourth root of the average plaquette.

The parameters used in the valence quarks and in generating correlation functions are listed in Table II. The valence light quarks are degenerate with the sea quarks, i.e., $am_l = am'_l$; the valence s quark masses are set to our best determination of the s quark mass on each ensemble, based on all of our analysis of the asqtad ensembles. In general $am_h < am'_h$. The heavy b quark Wilson fermions with SW lattice action are controlled by the hopping parameter κ and the clover coefficient of the SW action $c_{\rm sw}$. We use κ'_b to denote the values used in the computation. We use the tadpole-improved tree-level value for $c_{\rm sw} = u_0^{-3}$, with u_0 listed in Table I. The parameter d_1 is used for the correlation function generation and will be explained later in Sec. III C.

Table III lists the parameters derived from the lattice simulation. The relative lattice scale is set by calculating r_1/a on each ensemble, where r_1 is related to the force between static quarks, $r_1^2 F(r_1) = 1.0$ [59,60]. A mass-independent procedure is used to set r_1/a. We use the r_1/a to convert all lattice quantities to r_1 units. The physical value of r_1 is determined from f_π: $r_1 = 0.3117(22)$ fm [22,61]. The physical value κ_b [14], corresponding to the physical b-quark mass, and the critical value $\kappa_{\rm crit}$, corresponding to the zero quark masses in the SW action on each ensemble, are also listed in Table III. They will be used only for correcting the b-quark masses as will be discussed in Sec. IV C. The Goldstone pion mass M_π and the root-mean-square (rms) pion mass $M_\pi^{\rm rms}$ are listed in the last two columns of Table III.

[1]In this paper, we use primed quantities to denote the sea quarks and the unprimed for the valence quark.

C. Interpolating operators, currents, and correlation functions

Here we specify the interpolating operators for the kaon and B_s meson and the lattice vector current needed for the correlation functions in Eq. (3.8). For the kaon, the local pseudoscalar interpolating operator is used

$$\mathcal{O}_K(t,\boldsymbol{x}) = \bar{\chi}(t,\boldsymbol{x})(-1)^{t+x_1+x_2+x_3}\chi(t,\boldsymbol{x}), \tag{3.9}$$

where $\chi(t,\boldsymbol{x})$ is the one-component staggered fermion field.

The B_s meson interpolating operator contains a b-quark field, simulated with the improved Wilson action, and a light staggered field for the s-quark [11,62,63]

$$\mathcal{O}_{B_s}(t,\boldsymbol{x}) = \sum_{\boldsymbol{y}} \bar{\psi}(t,\boldsymbol{y}) S(\boldsymbol{y},\boldsymbol{x}) \gamma_5 \Omega(t,\boldsymbol{x}) \chi(t,\boldsymbol{x}), \tag{3.10a}$$

$$\Omega(t,\boldsymbol{x}) \equiv \gamma_1^{x_1}\gamma_2^{x_2}\gamma_3^{x_3}\gamma_4^{t}, \tag{3.10b}$$

where $\psi(t,\boldsymbol{y})$ is the four-component b-quark field, and $S(\boldsymbol{x},\boldsymbol{y})$ is a spatial smearing function. We use two smearing functions for the B_s meson. One is the local $S(\boldsymbol{x},\boldsymbol{y}) = \delta(\boldsymbol{x}-\boldsymbol{y})$. The other one is the ground-state 1S wave function of the Richardson potential [61].

The lattice vector current operator in Eqs. (3.7) and (3.8c) is defined as in Refs. [11,62]

$$V^\mu(x) = \bar{\Psi}(x)\gamma^\mu \Omega(x)\chi(x), \tag{3.11}$$

where the rotated b-quark field Ψ, defined by

$$\Psi = (1 + ad_1 \boldsymbol{\gamma}\cdot\boldsymbol{D}_{\rm lat})\psi, \tag{3.12}$$

removes $O(a)$ discretization effects from the current [48]. Here $\boldsymbol{D}_{\rm lat}$ is a symmetric nearest-neighbor covariant difference operator. The coefficient d_1, shown in Table II, is set to its tadpole-improved tree-level value so that the lattice vector current is tree-level $O(a)$ improved.

The renormalization constant Z_{V_μ}, needed to match the lattice vector current to its continuum counterpart [see Eq. (3.7)], is determined using a mostly nonperturbative renormalization procedure [64,65]:

$$Z_{V^\mu_{bl}} = \rho_{V^\mu}\sqrt{Z_{V^4_{bb}} Z_{V^4_{ll}}}, \tag{3.13}$$

where $Z_{V^4_{bb}}$ and $Z_{V^4_{ll}}$ are the renormalization factors for the flavor-diagonal b- and light-quark temporal vector currents that are calculated nonperturbatively in Ref. [16] and listed in Table IV. The remaining flavor-off-diagonal parameters ρ_{V^μ} are calculated to one-loop order in perturbation theory,

TABLE III. Parameters derived from the simulation. The approximate lattice spacing a in fm and the lattice dimensions in lattice units $N_s^3 \times N_t$ are used for identifying the ensemble. Relative scales r_1/a are listed in the third column. The statistical errors on r_1/a are 0.1 to 0.3% and the systematic errors are comparable. The physical κ_b [14] for the SW action are listed in the fourth column, where the first error is the statistics plus fitting error and the second one is due to the uncertainty in the lattice spacing. The critical κ_{crit} for the SW action are listed in the fifth column. The errors of κ_{crit} are in the last digit. We also list the Goldstone pion mass (M_π) and root-mean-square pion mass here.

≈a (fm)	$N_s^3 \times N_t$	r_1/a	κ_b	κ_{crit}	M_π (MeV)	M_π^{rms} (MeV)
0.12	$24^3 \times 64$	2.73859	0.0868(9)(3)	0.14096	277	456
0.09	$28^3 \times 96$	3.78873	0.0967(7)(3)	0.139119	354	413
0.09	$32^3 \times 96$	3.77163	0.0966(7)(3)	0.139134	307	374
0.09	$40^3 \times 96$	3.75459	0.0965(7)(3)	0.139173	249	329
0.09	$64^3 \times 96$	3.73761	0.0964(7)(3)	0.13919	177	277
0.06	$64^3 \times 144$	5.30734	0.1050(5)(2)	0.137678	224	255

separately from this analysis, and also listed in Table IV. In order to reduce subjectivity in our analysis, we employed a blinding procedure in the form of a small multiplicative offset applied to the ρ factors and known to only two of the authors. This blinding factor was subsequently disclosed and removed only after the analysis choices were finalized.

In the generation of the correlation functions defined in Eqs. (3.8), (3.9), (3.9), and (3.11), we increase statistics by repeating the calculation at N_{src} source times evenly distributed in the N_t direction. The three-point correlation functions are generated with two adjacent temporal source-sink separations: $T = T_{\text{sink}}$ and $T = T_{\text{sink}} + 1$. Both N_{src} and T_{sink} are listed in Table V. For the kaon recoil momenta we include the following lowest possible values: $\boldsymbol{p}_K/(2\pi/N_s) = (0,0,0),(1,0,0),(1,1,0),(1,1,1)$ and (2,0,0). In practice, the largest momentum $\boldsymbol{p}_K = 2\pi(2,0,0)/N_s$ is too noisy and is excluded from the analysis.

IV. ANALYSIS

With lattice correlation functions in hand, we follow the steps outlined near the end of Sec. III A to determine the form factors defined there, where we make use of the spectral decomposition of the correlation functions to extract the desired parameters. The two-and three-point functions take the form [62]

$$C_2^{B_s}(t;0) = \sum_{n=0}^{2N-1} (-1)^{n(t+1)} |Z_{B_s}^{(n)}|^2 (e^{-M_{B_s}^{(n)} t} + e^{-M_{B_s}^{(n)}(N_t - t)}), \tag{4.1a}$$

$$C_2^{K}(t;\boldsymbol{p}_K) = \sum_{n=0}^{2N-1} (-1)^{n(t+1)} |Z_K^{(n)}(\boldsymbol{p}_K)|^2 (e^{-E_K^{(n)} t} + e^{-E_K^{(n)}(N_t - t)}), \tag{4.1b}$$

$$C_{3,\mu}^{B_s \to K}(t,T;\boldsymbol{p}_K) = \sum_{m,n=0}^{2N-1} (-1)^{m(t+1)} (-1)^{n(T-t-1)} \left| Z_{B_s}^{(n)} \right| \times \left| Z_K^{(m)}(\boldsymbol{p}_K) \right| D_{mn}^{\mu} e^{-E_K^{(m)} t} e^{-M_{B_s}^{(n)}(T-t)}, \tag{4.1c}$$

with

TABLE IV. Parameters for the renormalization of the form factors. The approximate lattice spacing a and lattice dimensions $N_s^3 \times N_t$ in the first two columns identify the ensemble. The light-light and heavy-heavy renormalization factors $Z_{V_{ll}^4}$ and $Z_{V_{bb}^4}$ are listed in the third and fourth columns. The one-loop estimates of ρ_{V^i} and ρ_{V^4} are listed in the fifth and sixth columns. The errors shown are statistical. The complete current renormalization is obtained via Eq. (3.13).

≈a (fm)	$N_s^3 \times N_t$	$Z_{V_{ll}^4}$	$Z_{V_{bb}^4}$	ρ_{V^i}	ρ_{V^4}
0.12	$24^3 \times 64$	1.7410(30)	0.5015(8)	0.973082	1.006197
0.09	$28^3 \times 96$	1.7770(50)	0.4519(15)	0.975822	0.999308
0.09	$32^3 \times 96$	1.7760(50)	0.4530(15)	0.975775	0.999405
0.09	$40^3 \times 96$	1.7760(50)	0.4536(15)	0.975744	0.999441
0.09	$64^3 \times 96$	1.7760(50)	0.4536(15)	0.975703	0.999416
0.06	$64^3 \times 144$	1.8070(70)	0.4065(21)	0.979176	0.995327

TABLE V. The number of time sources N_{src} used in the two- and three-point correlation function generation and the source-sink separations T_{sink} used in the three-point correlation function generation. The approximate lattice spacing a and lattice dimensions $N_s^3 \times N_t$ in the first two columns identify the ensemble.

≈a (fm)	$N_s^3 \times N_t$	N_{src}	T_{sink}
0.12	$24^3 \times 64$	4	18
0.09	$28^3 \times 96$	4	25
0.09	$32^3 \times 96$	8	25
0.09	$40^3 \times 96$	8	25
0.09	$64^3 \times 96$	4	25
0.06	$64^3 \times 144$	4	36

$$Z_{B_s}^{(n)} = \frac{|\langle 0|\mathcal{O}_{B_s}|B_s{}^{(n)}\rangle|}{\sqrt{2M_{B_s}^{(n)}}}, \tag{4.2a}$$

$$Z_K^{(n)}(\boldsymbol{p}_K) = \frac{|\langle 0|\mathcal{O}_K|K^{(n)}(\boldsymbol{p}_K)\rangle|}{\sqrt{2E_K^{(n)}}}, \tag{4.2b}$$

$$D_{mn}^{\mu} \equiv \frac{\langle K^{(m)}|V^{\mu}|B_s^{(n)}\rangle}{\sqrt{2E_K^{(m)}}\sqrt{2M_{B_s}^{(n)}}}. \tag{4.2c}$$

The $(-1)^{n(t+1)}$ and $(-1)^{n(T-t)}$ terms in Eq. (4.1) arise because with our choice for the light-quark valence action the interpolating operators also generate opposite-parity (scalar) states. The overlap factors $Z_{B_s}^{(n)}$ and $Z_K^{(n)}(\boldsymbol{p}_K)$ describe the overlap of the interpolating operators with the states $|B_s{}^{(n)}\rangle$ and $|K^{(n)}(\boldsymbol{p}_K)\rangle$, respectively, while the D_{mn}^{μ} contain the desired matrix element.

In Sec. IV A, we extract the meson masses, and the overlap factors $Z_{B_s}^{(n)}$ and $Z_K^{(n)}(\boldsymbol{p}_K)$ from the two-point correlation functions. We explain how the lattice form factors are extracted from the two- and three-point correlation functions in Sec. IV B. We briefly describe the heavy b-quark mass corrections in Sec. IV C. The chiral-continuum fit function and extrapolation are described in Sec. IV D.

A. Analysis of the two-point correlation functions

The B_s-meson masses, kaon masses, kaon energies, and B_s and kaon overlap factors are obtained from fitting the two-point correlation functions to the functional forms in Eqs. (4.1a) and (4.1b).

As listed in Table V, there are 4 or 8 time sources for each ensemble. The two-point correlation functions are averaged together and folded around $N_t/2$ before constructing the ensemble-averaged propagators and covariance matrix required for the two-point function fits. We use Bayesian constraints with Gaussian priors to perform fits to the correlation functions which include excited states. We vary the number of states and range of time slices included in the fits to separate excited state contributions from the desired ground state parameters and obtain reliable estimates of the uncertainties. The lower end of the fit ranges t_{min} is chosen small enough to get a good handle on the excited states and to obtain a good correlated p value as defined in Ref. [66]. We choose the upper end of the fit ranges t_{max} such that the relative error does not exceed 3%, because we find that adding data at larger t values does not significantly affect the statistical errors or the quality of the fits. However, the resulting increase in the size of the covariance matrix makes it even more difficult to accurately determine the smallest eigenvalues (and corresponding eigenvectors) of the covariance matrix without significantly increasing the number of configurations we analyze. Similar conclusions were also obtained in Ref. [16]. The fit ranges $[t_{\mathrm{min}}, t_{\mathrm{max}}]$ for different lattice spacings are also adjusted so that the physical distances are similar. Our fit functions include the same number of opposite parity states as regular parity states. The number-of-states parameter N in Eq. (4.1) therefore refers to a fit function with the pseudoscalar ground state plus $N-1$ of its radial excitations and N scalar states. Our central value fits have $N = 3$. The prior central values for the ground state energies and overlap factors are guided by the effective mass and effective amplitude evaluated at large times t. The effective mass m_{eff} and effective amplitude Z_{eff} are constructed from the two-point correlation functions via

$$m_{\mathrm{eff}} \equiv -\log\left[C_2(t+1)/C_2(t)\right], \qquad Z_{\mathrm{eff}}^2 \equiv e^{+m_{\mathrm{eff}}t}C_2(t). \tag{4.3}$$

Here C_2 stands for the lattice two-point correlation function for the kaon or B_s meson. The prior central values for $M_{B_s}^{(0)}$, $M_K^{(0)} \equiv E_K^{(0)}$, $Z_{B_s}^{(0)}$, $Z_K^{(0)}(0)$, and $Z_K^{(0)}(\boldsymbol{p}_K)$ are set according to Eq. (4.3) and the widths are set to be 0.1 or larger in lattice units. The prior central values for $M_{B_s}^{(n\neq 0)}$ and $E_K^{(n\neq 0)}$ are set using the energy difference between ground states and the corresponding excited states from the PDG [67] values as a guide wherever available and the widths are set to be 0.1 or larger in lattice units. The prior central values for $Z_{B_s}^{(1)}$, $Z_K^{(1)}(0)$, and $Z_K^{(1)}(\boldsymbol{p}_K)$ are set using the $N = 1$ fit results as a guide and the widths are set to be 0.1 or larger in lattice units. The prior central values for $Z_{B_s}^{(2)}$, $Z_K^{(2)}(0)$, and $Z_K^{(2)}(\boldsymbol{p}_K)$ are set using $Z_{B_s}^{(0)}$, $Z_K^{(0)}(0)$, and $Z_K^{(0)}(\boldsymbol{p}_K)$ as a guide and the widths are set to be 0.1 or larger in lattice units. Finally the prior central values for $Z_{B_s}^{(3,4,5)}$, $Z_K^{(3,4,5)}(0)$, and $Z_K^{(3,4,5)}(\boldsymbol{p}_K)$ are set to be 0.1 and the widths are set to be 1.0 or larger in lattice units. In summary, our choices for the prior widths are guided by previous experience [16,18] and we find that they are large enough so that no bias is introduced in the fits as illustrated in Fig. 2. An example of the B_s effective mass, prior, and fit result is shown in the left panel of Fig. 2. The corresponding kaon effective mass has smaller oscillations and much smaller errors as shown in the right panel of Fig. 2.

As illustrated in Fig. 3, our fit results are stable over a range of t_{min} choices and we find that they are consistent with results from $N = 2$ fits. The lattice correlation functions are precise enough to determine the first excited and opposite-parity, $N = 2$, states. Including extra $N = 3$ excited states better stabilizes the errors of fit posteriors. The left panel of Fig. 3 shows an example of the stability plot for the B_s meson. Fit intervals are chosen based on

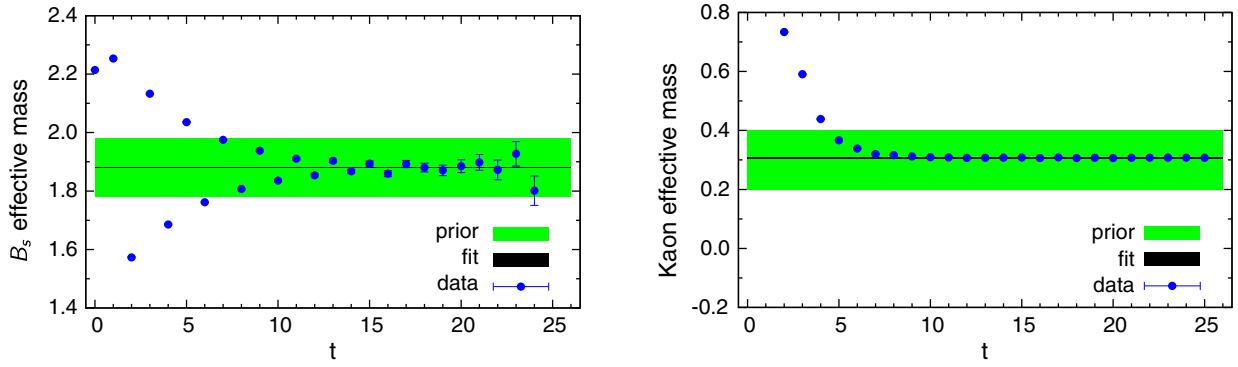

FIG. 2. B_s and kaon meson two-point correlation function for the $a \approx 0.12$ fm, $N_s^3 \times N_t = 24^3 \times 64$ ensemble. The blue points are the effective mass constructed via Eq. (4.3). The prior is shown as a green band. The fitted meson mass is shown as a thin gray horizontal band. Some of the blue-point error bars are too small to be visible. The error of the fitted kaon meson mass is magnified 20 times to make it visible in the plot.

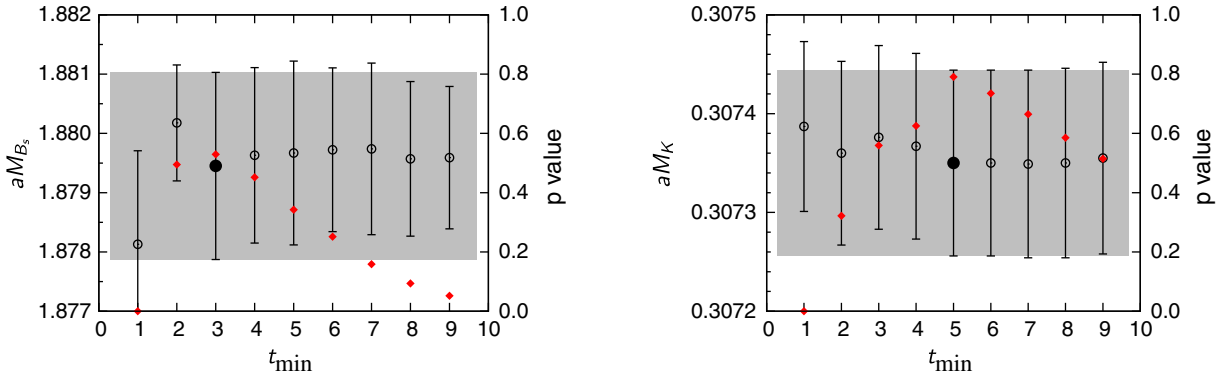

FIG. 3. Fitted B_s-meson and kaon masses, M_{B_s} and M_K in lattice units at different t_{min} for the $a \approx 0.12$ fm, $N_s^3 \times N_t = 24^3 \times 64$ ensemble. The left vertical axes show the fitted masses and the right vertical axes show the corresponding p value of the fit. The chosen fit results are shown in wide gray bands. The masses are shown in circles with error bars. The selected value of t_{min} is plotted using a solid circle and its error band is extended across the plot in gray. Red diamonds denote the p values.

these plots and are listed in Table VI. Representative fit results for the kaon are shown in the right panel of Fig. 3.

The fit results for the kaon energies and overlap factors can be compared with the continuum relations

$$E_K^2 = M_K^2 + \boldsymbol{p}_K^2, \qquad Z_K^{(0)}(\boldsymbol{p}_K) = Z_K^{(0)}(0)\sqrt{\frac{M_K}{E_K}} \tag{4.4}$$

to study momentum-dependent discretization errors. As illustrated in Fig. 4, we find that the E_K and $Z_K^{(0)}(\boldsymbol{p}_K)$ satisfy Eq. (4.4) albeit with increasing statistical errors at higher momenta. We therefore use the continuum relations for the kaon energies and Z_K factors whenever possible.

TABLE VI. Fit ranges $[t_{\mathrm{min}}, t_{\mathrm{max}}]$ used in the kaon and B_s meson two-point correlator fits.

≈a (fm)	Kaon	B_s meson
0.12	[5,31]	[3,22]
0.09	[7,47]	[4,30]
0.06	[10,71]	[6,44]

B. Extracting form factors from two- and three-point correlation functions

The form factors are related to the semileptonic matrix elements via Eq. (3.6), and the lattice matrix elements are contained in the three-point correlation function as in Eqs. (4.1c) and (4.2). To get the lattice form factors $f_{\parallel,\perp}^{\mathrm{lat}}$, we fit the two- and three-point correlation functions together. In particular, we perform combined two- and three-point correlation-function fits according to Eqs. (4.1) and (4.2) with $N = 3$. The three-point fit ranges are chosen to be $[t_{\mathrm{min}}^K, T - t_{\mathrm{min}}^{B_s}]$ with $T = T_{\mathrm{sink}}$ or $T_{\mathrm{sink}} + 1$. The parameters to be fitted are $M_{B_s}^{(n)}$, $E_K^{(n)}$, $Z_{B_s}^{(n)}$, $Z_K^{(n)}(\boldsymbol{p}_K)$, and D_{mn}^{μ}. The prior central values for the B_s-meson and kaon masses, $Z_{B_s}^{(0)}$, and $Z_K^{(0)}(\boldsymbol{p}_K)$ are chosen as the posteriors of the two-point correlator fits. The kaon energies and $Z_K^{(0)}(\boldsymbol{p}_K)$ are constrained according to Eq. (4.4). The $Z_{B_s}^{(n\neq 0)}$ and

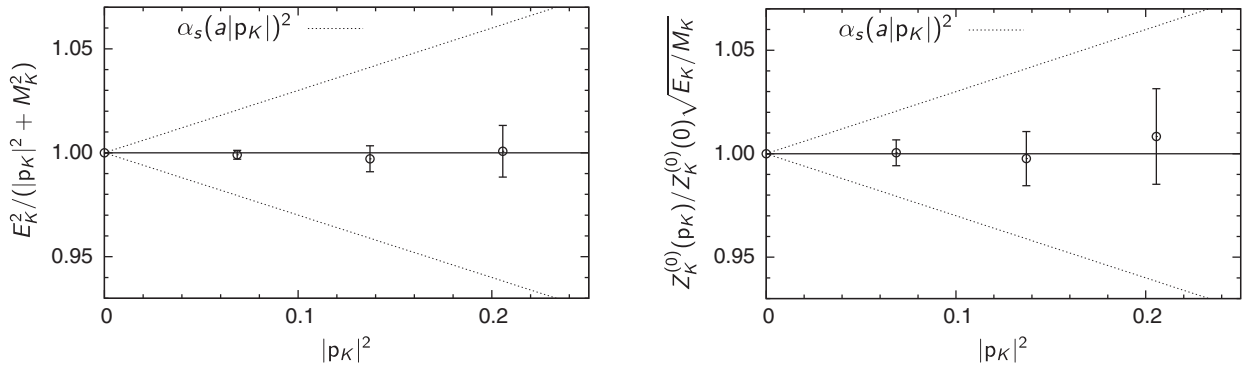

FIG. 4. Test of Eq. (4.4) for the $a \approx 0.12$ fm, $N_s^3 \times N_t = 24^3 \times 64$ ensemble. Left: energy-momentum dispersion relation where E_K and M_K come from the kaon 2-point correlators. Right: test of wave function overlap momentum dependence. The dashed lines on both plots show the power-counting estimate of the size of the momentum-dependent discretization error, $\mathcal{O}(\alpha_s|\boldsymbol{p}_K|^2 a^2)$.

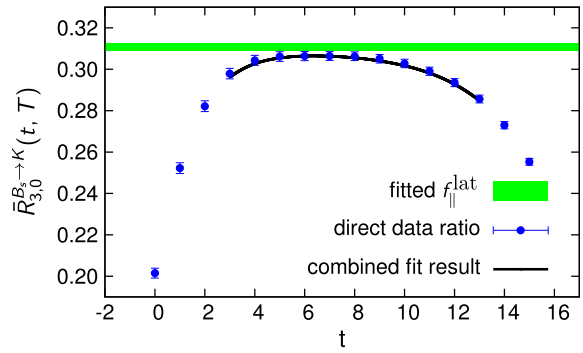

FIG. 5. The lattice form factor from a combined two-point and three-point correlation function fit for the $a \approx 0.12$ fm, $N_s^3 \times N_t = 24^3 \times 64$ ensemble. The green band is the combined fit result for $f_\parallel{}^{\rm lat}$. The blue points with errors are obtained from the ratio defined in Refs. [16,18]. The black curve is the ratio constructed directly from combined fit results. The small difference between the green band and the ratio comes from excited state contributions still present in the ratio but accounted for in the fit method used here.

$Z_K^{(n\neq 0)}(\boldsymbol{p}_K)$ central values are taken to be the same size as $Z_{B_s}^{(0)}$ and $Z_K^{(n\neq 0)}(0)$. The priors for D_{00}^{μ} are guided by the constructed ratio $\bar{R}_{3,0}^{B_s\to K}(t, T)$ defined in Refs. [16,18]. The prior widths for the above parameters are chosen to be 0.1 or larger in lattice units. The priors for all the other D_{mn}^{μ} are chosen to be 0.1 ± 2.0. The ground-state energies obtained from the combined two- and three-point correlator fits are consistent with those from the two-point fits as described in Sec. IV A.

Figure 5 shows that the fitted $f_\parallel{}^{\rm lat}$ coming from the combined fit is in slight tension with the constructed ratio $\bar{R}_{3,0}^{B_s\to K}(t, T)$ defined in Refs. [16,18]. This small difference comes from excited state contributions still present in the ratio but accounted for in the fit method used here. We find that they are significant at the present level of precision. Figure 6 shows an example of the stability of the fit result when varying the fit range.

In summary, the form factors $f_\parallel$ and $f_\perp$ are obtained from D_{00}^{μ} and E_K according to Eqs. (3.6) and (4.2c), after adding the renormalization factors as in Eq. (3.6).

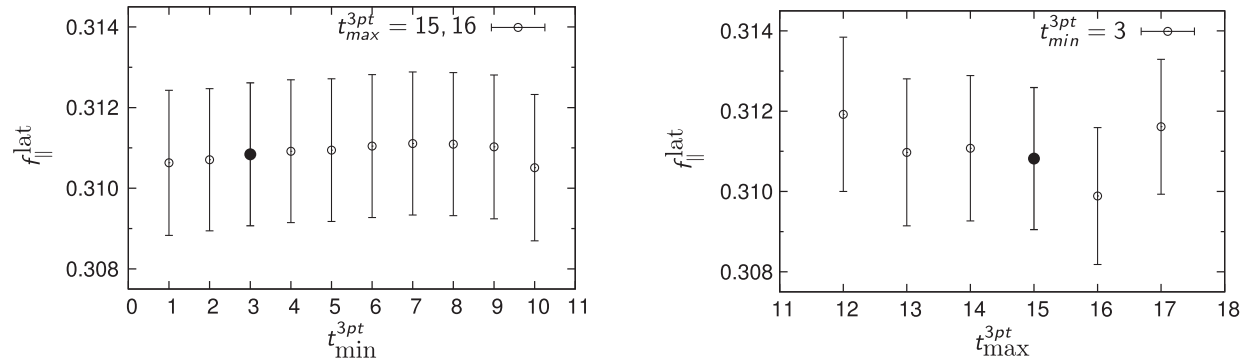

FIG. 6. Fit results of $\langle K^{(0)}|V^0|B_s^{(0)}\rangle$ from different fit ranges for the $a \approx 0.12$ fm, $N_s^3 \times N_t = 24^3 \times 64$ ensemble with lattice kaon momentum $\boldsymbol{p}_K = (2\pi/N_s)(0, 0, 0)$. Left: The three-point correlator fit maximum are fixed to be $t_{\rm max}^{\rm 3pt} = 15$ and 16 and the minimum are varied between 1 and 10. Right: The three-point correlator fit minimum are fixed to be $t_{\rm min}^{\rm 3pt} = 3$ and the maximum is varied between 12 and 17. The preferred fit ranges are shown with filled points.

C. Heavy bottom quark mass correction

The heavy valence b quark is simulated with the Sheikholeslami-Wohlert (SW) action [47] with the Fermilab interpretation [48]. The b-quark mass is controlled by the hopping parameter κ_b. The hopping parameter κ_b' used in the simulations differs slightly from the physical value κ_b as can be seen in Tables II and III. We need to correct the form factors to account for these small shifts. A detailed description of the κ tuning analysis and results is provided in Appendix C of Ref. [14]. We use the method described in Refs. [16,18] to adjust the form factors to account for the slightly mistuned values of κ_b. The relative change in the form factors under small variations of the b-quark mass can be described as

$$f(m_2') = f(m_2)\left[1 - \frac{\partial \ln f}{\partial \ln m_2}\left(\frac{m_2}{m_2'} - 1\right)\right], \quad (4.5)$$

where m_2 is the physical b-quark kinetic mass, m_2' is the b-quark mass used in the production run. The slopes $\frac{\partial \ln f}{\partial \ln m_2}$ were determined in Ref. [16]. The corrections to the form factors are about 0.1%–1.8% on different ensembles.

D. Chiral-continuum extrapolation

The lattice form factors extracted from the correlation functions as described in Sec. IV B are obtained at the three finite lattice spacings and unphysical light-quark masses listed in Table I. Here we extrapolate them to the continuum limit and physical light-quark masses using SU(2) hard-kaon heavy-meson rooted staggered chiral perturbation theory (HMrSχPT) [68,69]. Based on previous experience with the analyses of similar processes in Refs. [16,18], this best describes the data. Heavy-quark discretization effects are also taken into account in the chiral-continuum extrapolation.

We employ the HMrSχPT expansion at next-to-leading order in SU(2), leading order in $1/M_B$, where M_B is the B-meson mass, and include next-to-next-to-leading-order (NNLO) analytic and generic discretization terms. In the SU(2) hard-kaon limit, the valence and sea s-quark masses are taken to be infinitely heavy and hence dropped from the HMrSχPT formula; the large kaon energy is integrated out, and its effects are absorbed into the low-energy constants (LECs). In Ref. [18], the conversion rules for $B \to K$ and $B \to \pi$ processes from SU(3) HMrSχPT to SU(2) hard-kaon and hard-pion limits were derived. Here we follow the same procedure to obtain the corresponding formula for $B_s \to K\ell\nu$. The details are presented in Appendix A.

The NLO expression for $B_s \to K\ell\nu$ form factors in the SU(2) hard-kaon limit that we obtain is

$$f_{P,\mathrm{NLO}} = f_P^{(0)}\Big[c_P^0(1 + \delta f_{P,\mathrm{logs}}^{\mathrm{SU(2)}}) + c_P^1\chi_l + c_P^2\chi_{\mathrm{h}} + c_P^3\chi_E + c_P^4\chi_E^2 + c_P^5\chi_{a^2}\Big], \quad (4.6)$$

where $P = \parallel$ or $\perp$, $\delta f_{P,\mathrm{logs}}^{\mathrm{SU(2)}}$ are the nonanalytic contributions from the light-quark mass and lattice spacing, and the χ variables are dimensionless. They are defined in Eqs. (A3) and (A7). The leading-order factor is

$$f_P^{(0)} = \frac{1}{f_\pi}\frac{g_\pi}{E_K + \Delta_P^*}, \quad (4.7)$$

where f_π is the decay constant involved, and g_π is the $B^*B\pi$ coupling constant.[2] The Δ_P^* term takes the pole contribution into account and is determined by requiring $f_\parallel$ and $f_\perp$ to have the same poles as the physical form factors f_0 and f_+, respectively. This is reasonable because, by Eq. (3.5), $f_\parallel$ is dominated by the 0^+ contributions of f_0, and $f_\perp$, by the 1^- contributions of f_+ in the q^2 range considered. Using Eq. (3.2), one obtains the exact expression for Δ_P^*:

$$\Delta_P^* = \frac{M_{B^*}^2 - M_{B_s}^2 - M_K^2}{2M_{B_s}}. \quad (4.8)$$

The vector meson (with $J^P = 1^-$) has been experimentally measured [5] to be $M_{B^*} = 5324.65(25)$ MeV; the scalar B^* meson (with $J^P = 0^+$) has not been observed experimentally, but a lattice calculation [70] estimates the mass difference between 0^+ and 0^- states to be around 400 MeV:

$$M_{B^*}(0^+) - M_B \approx 400\ \mathrm{MeV}. \quad (4.9)$$

The vector-meson mass M_{B^*} is below the $B\pi$ production threshold that is involved in the $B_s \to K\ell\nu$ decay, and the scalar-meson mass $M_{B^*}(0^+)$ is above the threshold. The inclusion of the scalar pole and its exact location have little impact on the chiral fit results but stabilizes the form factor extrapolations.

NNLO analytic terms are included in the fits to take into account higher-order contributions. The leading heavy b-quark discretization effects are also included. The expressions for the NNLO fit functions are

$$f_{P,\mathrm{NNLO}} \equiv f_{P,\mathrm{NNLO+HQ}} = (f_{P,\mathrm{NLO}} + f_P^{(0)}\delta f_{\mathrm{NNLO}}) \times (1 + \delta f_{\mathrm{HQ}}), \quad (4.10a)$$

$$\delta f_{\mathrm{NNLO}} = c_P^6\chi_l\chi_E + c_P^7\chi_{a^2}\chi_E + c_P^8\chi_E^3 + c_P^9\chi_l^2 + c_P^{10}\chi_l\chi_E^2 + c_P^{11}\chi_{a^2}\chi_l + c_P^{12}\chi_{a^2}\chi_E^2 + c_P^{13}\chi_{a^2}^2 + c_P^{14}\chi_E^4, \quad (4.10b)$$

$$\delta f_{\mathrm{HQ}} = (h_P^1 f_E + h_P^2 f_X + h_P^3 f_Y)(a\Lambda)^2 + (h_P^4 f_B + h_P^5 f_3)(\alpha_s a\Lambda) + h_P^6\alpha_s(a\Lambda)^2, \quad (4.10c)$$

[2] SU(3) breaking effects renormalize the g_π/f_π ratio; however, since it results in a overall multiplicative factor, it has been reabsorbed in the fitting coefficients.

TABLE VII. Priors used in the chiral-continuum extrapolation fit. c_p^{NLO} represents $c_P^0, \ldots, c_P^5$ as shown in Eq. (4.6). c_p^{NNLO} represents $c_P^6, \ldots, c_P^{14}$ as shown in Eq. (4.10b). h_P represents $h_P^1, \ldots, h_P^6$ as appears in Eq. (4.10c).

f_π	g_π	c_P^{NLO}	c_P^{NNLO}	h_P
130.4 MeV	0.45(8)	0(1.0)	0(0.6)	0(1.0)

where the heavy-quark discretization effects are modeled with δf_{HQ}. The mismatch functions $f_{E,X,Y,B,3}$ are defined in the appendix of Ref. [61]. The next-to-leading-order analytic term $f_{P,\mathrm{NLO}}$ was defined previously in Eq. (4.6). A Bayesian method is used in the chiral-continuum fit. The priors are listed in Table VII. The fit results using the NNLO fit function in Eq. (4.10) are used as the central fit and are shown in Fig. 7.

V. SYSTEMATIC ERROR ESTIMATIONS

The chiral-continuum extrapolated form factors are given in Sec. IV. The statistical-fit errors, which are propagated through each step of the analysis already include the effects of NNLO terms in the chiral expansion as well as light- and heavy-quark discretization. Here we discuss tests of the robustness of this error estimate to check for the presence of residual truncation effects. We also consider other sources of error not already included in our chiral-continuum fit function and construct a complete systematic error budget over the range of q^2 for which we have lattice data, 19 $\mathrm{GeV}^2 \lesssim q^2 \lesssim 24\ \mathrm{GeV}^2$.

A. Chiral-continuum extrapolation errors

Our central fit uses the NNLO SU(2) hard kaon HMrSχPT fit function described in Eq. (4.10). In order to study truncation effects, we consider variations of the central fit function. We also perform fits which include fewer form factor data.

We estimate chiral truncation effects by comparing our central NNLO fit with fits using either only the NLO function, defined in Eq. (4.6), or a fit function that includes the complete set of next-to-NNLO (NNNLO) terms. The coefficients of the NNNLO terms are constrained with the same priors as the NNLO ones. Figure 8 shows the comparison of results for the f_+ form factor from the three fits. The corresponding results for f_0 are similar. We see that the results from the three different fits are consistent with each other over the range of q^2 where the simulation data are located. The NNNLO errors at small q^2 are larger since the data points in that region are scarce as can be seen in Fig. 7, and the fits cannot determine the higher order terms accurately. The truncation errors are well saturated in the $q^2 \gtrsim 19\ \mathrm{GeV}^2$ region, and therefore it is unnecessary to add an additional systematic error.

The SU(2) hard-kaon formula is used for the central fit. To see how other choices of the HMrSχPT formula affect the fits, we performed the fit with soft-kaon HMrSχPT. The resulting difference is small, especially for the f_+ form factor. This can be seen in Fig. 9. Since the valence s-quark masses are not equal to the sea ones, the corresponding SU(3) HMrSχPT formulas are extremely complicated.

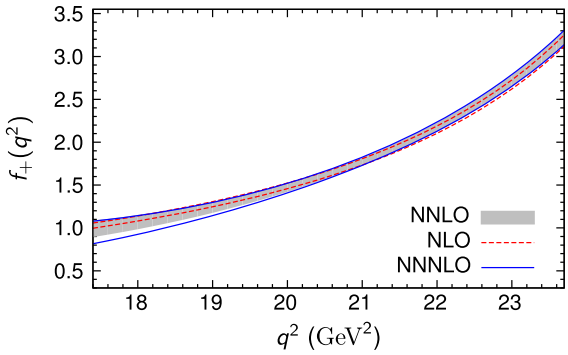

FIG. 8. Comparison among chiral-continuum extrapolated results for f_+ with different analytic terms. The gray band shows the preferred fitting result with NNLO SU(2) HMrSχPT. The red (dashed) and blue (solid) curves show the error ranges resulting from the fits with only NLO analytic terms and with all terms up to NNNLO, respectively.

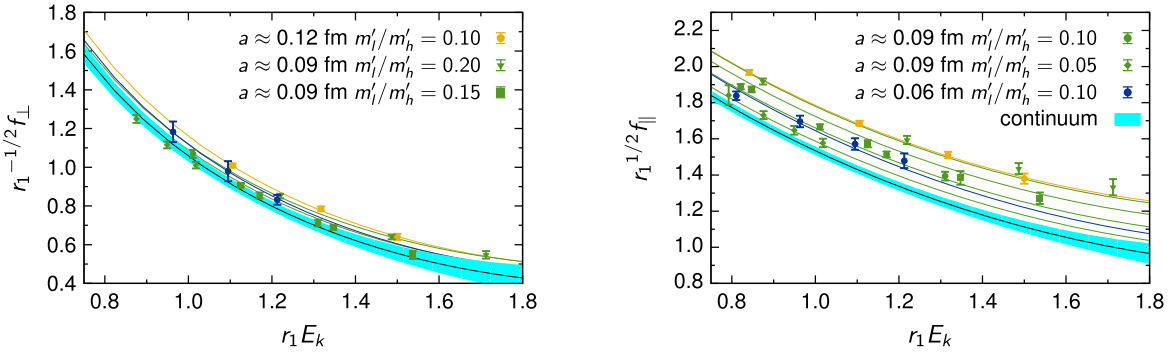

FIG. 7. Chiral-continuum extrapolated form factors $f_\parallel$ and $f_\perp$ in r_1 units as functions of the recoil energy $r_1 E_K$. The color denotes the lattice spacings and the symbols denote the ratio of the sea-quark masses m_l'/m_h'. The colored fit lines correspond to the fit results evaluated at the parameters of the ensembles. The cyan band with the black curve shows the chiral-continuum extrapolated results.

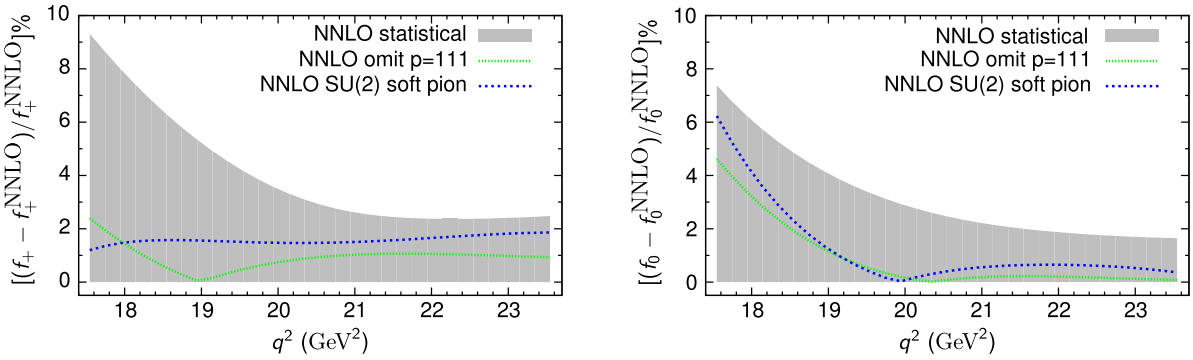

FIG. 9. Percent deviations of alternative chiral-continuum extrapolations from the preferred central fit of f_+ and f_0. The curves show the deviation from the preferred central fit obtained by either omitting the $\boldsymbol{p}_K = 2\pi(1,1,1)/N_s$ data points or by using SU(2) soft pion HMrSχPT formula. The gray band shows the statistical errors from the preferred NNLO SU(2) HMrSχPT fits. The deviations are smaller than the statistical errors.

We therefore did not perform any trial fits with the SU(3) formula. Nevertheless, from previous experience, [16,18], SU(3) HMrSχPT typically does not provide a good description of the data.

Our results with kaon momentum up to $2\pi(1,1,1)/N_s$ are used in the central chiral fit. To check how the kaon energy range affects the results, we perform the fit omitting the $\boldsymbol{p}_K = 2\pi(1,1,1)/N_s$ data. The differences are shown in Fig. 9. Again, the difference is small especially for the f_+ form factor and also for f_0 at $q^2 \gtrsim 19$ GeV^2.

Based on the tests discussed above and visually summarized in Figs. 8 and 9, we find that the deviations between the results from the central fit and the alternative fits are smaller than the statistical error of the preferred central fit. We therefore do not assign additional systematic errors due to these sources.

B. Current renormalization uncertainties

The mostly nonperturbative renormalization procedure, described in Eq. (3.7), used to renormalize the matrix elements (and hence the form factors) requires, as inputs, the factors $Z_{V^4_{bb}}$, $Z_{V^4_{ll}}$, ρ_{V^4}, and ρ_{V^i}. We estimate the error on $f_\parallel, f_\perp$ due to the uncertainties of the nonperturbatively determined $Z_{V^4_{bb}}$ and $Z_{V^4_{ll}}$ by varying their central values by 1 standard deviation in each direction. As expected, the resulting changes in the form factors are small, yielding errors on $f_\parallel, f_\perp$ in the range of 0.2%–0.3%.

For ρ_{V^4} and ρ_{V^i}, the dominant source of error is the truncation at one-loop order in perturbation theory. As seen in Table IV, the one-loop corrections provided by ρ_{V^4} and ρ_{V^i} are small, with ρ_{V^4} (ρ_{V^i}) deviating from unity by less than 1% (2.4%). Here, we adopt the estimate of the perturbative truncation error presented in Ref. [16], which yields an uncertainty of 1% on both ρ_{V^4} and ρ_{V^i}. This estimate is consistent with the observed differences between nonperturbative [71] and perturbative [72] calculations of $\rho_{V^4} = \rho_{A^4}$, discussed in Ref. [71]. In particular, the observed differences decrease in the continuum limit, as expected. Note, however, that the nonperturbative result [71] employs the HISQ action for the light quarks, while our one-loop results [72] employ the asqtad action. For this reason, the comparison is suggestive but not definitive.

C. Lattice-scale uncertainties

The dimensionful form factors $f_\perp$ and $f_\parallel$, and meson energies and masses are converted to physical units via the relative scales r_1/a listed in Table III and the absolute scale $r_1 = 0.3117(22)$ fm [61]. The statistical errors on r_1/a are small and their effects on the form factors can be neglected. We estimate the error due to the uncertainty of r_1, as before, by shifting its value by 1 standard deviation and repeating the chiral fit. The shifts on the form factors $f_{+,0}$ are at most 0.8% in the range of simulated momenta.

D. Quark mass uncertainties

The continuum physical form factors are obtained by evaluating the chiral-continuum extrapolated functions, as discussed in Sec. IV D at the physical averaged u- and d-quark masses, namely, $r_1 m_{ud}^{\rm phys} = 0.000965(33)$, and the physical s-quark mass $r_1 m_s^{\rm phys} = 0.0265(8)$ as determined by analyzing the light pseudoscalar meson spectrum [22]. The error due to the uncertainties in these masses is obtained by varying their central values by 1 standard deviation to find the corresponding changes in the form factors. The maximum changes are below 0.15% in the simulated q^2 region.

E. Uncertainties arising from the bottom quark mass correction

As explained in Sec. IV C, the form factors are adjusted to account for the slightly mistuned valence b-quark masses before the chiral-continuum extrapolation. This accounts for the dominant effect from b-quark mass mistuning. The errors on the form factors due to the uncertainties in the

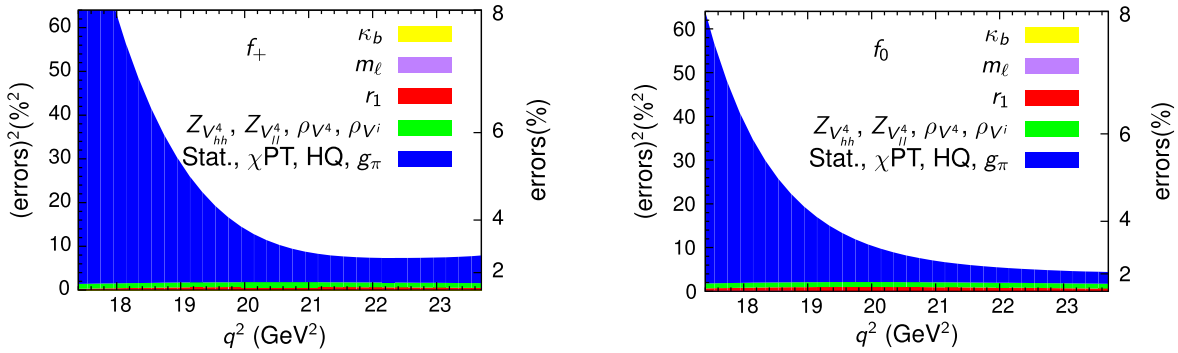

FIG. 10. Distribution of the errors for f_+ (left) and f_0 (right) as a function of q^2. The left y axis shows the square of the errors added in quadrature. The right y axis shows the errors themselves. The different bands show the total error when adding individual sources of error in quadrature one by one. The error bands associated with κ_b and m_ℓ are too small to be visible on the plots.

κ_b-correction factors and the tuned κ_b values are taken into account by following the procedure described in Ref. [16]. A q^2-independent 0.4% error due to tuning κ_b is assigned to both f_+ and f_0.

F. Finite volume effects

Finite-volume effects, estimated by comparing infinite-volume integrals with finite sums in HMrSχPT, are negligibly small [16,18], so they are omitted from the total error budget.

G. Summary of the statistical and systematic error budgets

The systematic errors discussed in this section are summarized in Fig. 10. We see that the largest source of systematic uncertainty by far comes from the chiral-continuum extrapolation, which includes higher-order discretization effects. This is especially obvious at small q^2, i.e., large $r_1 E_K$, because the statistical errors of the correlations functions increase with increasing recoil momentum so that the corresponding form factors at large $r_1 E_K$ have large errors. This is also due to a lack of data points in the large $r_1 E_K$ region as shown in Fig. 7. Furthermore, the HMrSχPT used to perform the extrapolation is valid only for moderate E_K. This is a generic feature common to all similar lattice calculations. Our aim, however, is to get the form factor in the whole kinematically allowed region, all the way to $q^2 = 0$. In the next section, Sec. VI, we will describe how the extrapolation can be done by including physical information to control the error in the small q^2 region.

The subdominant errors, excluding the chiral-continuum extrapolation error, have mild q^2 dependence. Following Ref. [16] we therefore treat them as constants in q^2 when propagating them to the z-parametrization fit in Sec. VI B. We conservatively take the maximum estimated error from each source in the simulated q^2 range and add them in quadrature. Specifically, the overall additional systematic error is 1.4% for both f_+ and f_0, which is added to the covariance function of the chiral-continuum fit using the procedure described in Ref. [16] prior to the next step in the analysis described in the following section.

VI. CONTINUUM FORM FACTORS

The continuum form factors obtained from the chiral-continuum extrapolations described in the previous two sections are reliable only in the high momentum transfer $q^2 \gtrsim 17$ GeV^2 region. In this section, we use a model-independent parametrization and expansion, namely, the z parametrization, to extrapolate the form factors to the whole kinematically allowed region. This parametrization and expansion is based on the analyticity of the form factors and angular momentum conservation. The parametrization we used was introduced by Bourrely, Caprini, and Lellouch (BCL) [73] and the fitting procedure and extrapolation technique was first introduced in our previous $B \to \pi\ell\nu$ paper [16].

In Sec. VI A, we briefly review the z parametrization and give the expansion form used in the analysis. In Sec. VI B, we present the extrapolated continuum form factors in the whole kinematically allowed region. The results are shown in Table X, and Figs. 12 and 13. A comparison with results of other groups is presented in Sec. VI C.

A. z parametrization of form factors

Before discussing the details of the method, let us first consider the properties of the semileptonic form factors. Causality and unitarity [74] imply that the $B_s \to K\ell\nu$ semileptonic form factors are real analytic functions[3] in the complex q^2 plane with a cut from $q^2 > t_{\rm cut}$ to ∞,

[3]An analytic function $f(x)$ is real analytic if it satisfies $f(x^*) = (f(x))^*$. If $f(x)$ is a real analytic function with a branch point at x_0, then $f(x)$ is real for $x < x_0$ and its discontinuity across the cut is purely imaginary: $f(x + i\epsilon) - f(x - i\epsilon) = 2i\mathrm{Im}f(x + i\epsilon)$.

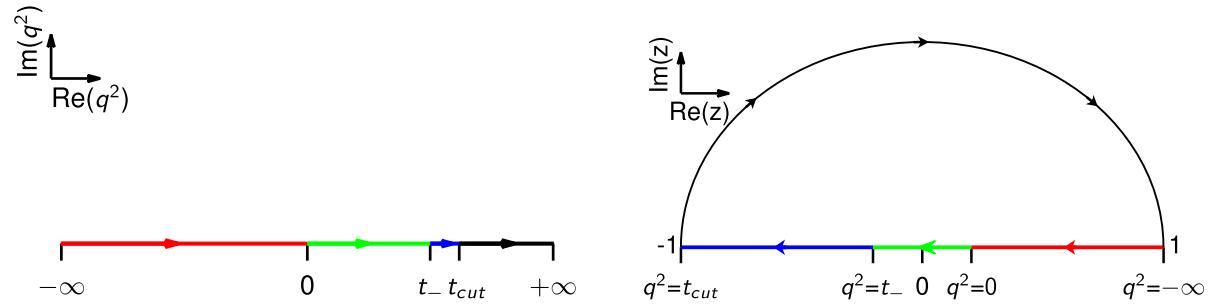

FIG. 11. A schematic diagram of the conformal mapping of the form factor regions from the complex q^2 plane to the complex z plane.

except at physical poles below $t_{\rm cut}$. The parameter $t_{\rm cut}$ is the particle-pair-production threshold. For $B_s \to K\ell\nu$, this is

$$\sqrt{t_{\rm cut}} = M_{B^+} + M_{\pi^0} = 5.414\ \text{GeV}. \tag{6.1}$$

The pole for the vector form factor is below the cut; while the one for the scalar form factor is above it. The above-threshold pole corresponds to an unstable particle, or resonance, and may appear only on the second Riemann sheet.

From deep-inelastic-scattering experiments and perturbative QCD scaling [75,76], it is known that the semileptonic form factors vanish rapidly as $1/q^2$, up to logarithmic corrections, when q^2 approaches minus infinity.

Near the threshold $t_{\rm cut}$, the form factors have the following scaling behavior

$$\text{Im}f_l(q^2) \sim (q^2 - t_{\rm cut})^{\frac{2l+1}{2}}, \tag{6.2a}$$

$$\text{Re}f_l(q^2) \sim a_l + b_l(q^2 - t_{\rm cut}), \tag{6.2b}$$

with $l = 0$ for f_0 and $l = 1$ for f_+, obtained from simple partial wave analysis.

Now let us look at the z parametrization. The z parametrization involves a conformal mapping. Conventionally, the variable q^2 is mapped to a new variable z according to

$$z(q^2, t_0) = \frac{\sqrt{t_{\rm cut} - q^2} - \sqrt{t_{\rm cut} - t_0}}{\sqrt{t_{\rm cut} - q^2} + \sqrt{t_{\rm cut} - t_0}}, \tag{6.3}$$

where t_0 is a parameter that can be chosen to optimize the mapping. The maximum momentum transfer allowed in the semileptonic $B_s \to K\ell\nu$ decay is defined as

$$t_- = (M_{B_s} - M_K)^2 \tag{6.4}$$

for convenience. This conformal mapping was first considered in Ref. [77] and further developed and used to get model-independent constraints, usually called "unitarity bounds," on form factors in Ref. [78]. A stronger constraint based on heavy-quark power counting was derived in Ref. [79]. The conformal transformation Eq. (6.3) maps the physical semileptonic region $0 \le q^2 \le t_-$ onto a small region on the real z axis, the upper edge of the cut onto the upper edge of the unit circle, the lower edge of the cut onto the lower edge of the unit circle, the limiting points $q^2 = \pm\infty$ to $z = 1$, and $q^2 = t_{\rm cut}$ to $z = -1$. The complex q^2 cut plane is mapped onto the unit disk in the z plane with the cut mapping onto the unit circle. The parameter t_0 can be chosen such that the semileptonic region is centered around $z = 0$ after the conformal mapping. This is obtained by solving the equation

$$z(q^2 = 0, t_0) = -z(q^2 = t_-, t_0). \tag{6.5}$$

The solution for t_0 is

$$t_0 = t_{\rm cut} - \sqrt{t_{\rm cut}(t_{\rm cut} - t_-)}. \tag{6.6}$$

This mapping is schematically shown in Fig. 11 with small lepton masses ignored and with the optimized t_0 as defined in Eq. (6.6).

Under the above transformation, the form factors are always in the region where $|z| < 1$, and therefore they can be parametrized as a power series in z. Since the physical semileptonic region in terms of z is usually small, $|z| \le 0.205$ for $B_s \to K\ell\nu$, this parametrization converges quickly. Table VIII has a list of quantities in terms of r_1E_K, q^2, and z parameters.

Two commonly used parametrizations are given by Boyd, Grinstein, and Lebed (BGL) [80] and by BCL [73]. Here we use the BCL parametrization as given by

$$f_+(q^2) = \frac{1}{1 - q^2/m^2_{B^*(1^-)}} \sum_{k=0}^{K-1} b_k^+(t_0) \left[z^k - (-1)^{k-K} \frac{k}{K} z^K \right], \tag{6.7a}$$

$$f_0(q^2) = \frac{1}{1 - q^2/m^2_{B^*(0^+)}} \sum_{k=0}^{K-1} b_k^0(t_0) z^k. \tag{6.7b}$$

The factors $1/(1 - q^2/m^2_{B^*})$ take the poles into account and ensure the asymptotic scaling, $f(q^2) \sim 1/q^2$ at large q^2. Moreover, the scaling condition of Eq. (6.2) near $t_{\rm cut}$ is

TABLE VIII. Quantities in terms of different parameters.

	$r_1 E_K$	$q^2(\mathrm{GeV}^2)$	z
Lattice data range	[0.846, 1.71]	[17.4, 23.3]	$[-0.186, -0.0174]$
Physical range	[0.780, 4.28]	[0, 23.7]	$[-0.205, 0.205]$
$t_- = (M_{B_s} - M_K)^2$	0.780	23.7	−0.205
$t_{\mathrm{cut}} = (M_B + M_\pi)^2$	−0.0395	29.3	−1.0
$t_0 = t_{\mathrm{cut}} - \sqrt{t_{\mathrm{cut}}(t_{\mathrm{cut}} - t_-)}$	1.84	16.5	0.0
$M^2_{B^*}(1^-)$	0.102	28.4	−0.569
$M^2_{B^*}(0^+)$	−0.473	32.3	$-0.625 + 0.781i$

also enforced for f_+. Note that Eq. (6.2) in the q^2 plane implies the following relations

$$\left.\frac{df_+}{dz}\right|_{z=-1} = \left.\frac{df_+}{dk}\frac{dk}{dz}\right|_{k=0} = 0, \tag{6.8a}$$

$$\left.\frac{df_0}{dz}\right|_{z=-1} = \left.\frac{df_0}{dk}\frac{dk}{dz}\right|_{k=0} = \text{const.} \tag{6.8b}$$

The form factors constructed with this BCL z parametrization satisfy all three properties of the semileptonic form factors discussed at the beginning of this section.

B. z-parametrization fit and extrapolation

We use Eq. (6.7) to perform the z-parametrization fit to our chiral-continuum-extrapolated form factor results obtained in Secs. IV D and V. The vector pole $M_{B^*(1^-)}$ is taken to be $M_{B^*(1^-)} = 5.32465(25)$ GeV [5], and the above threshold scalar pole $M_{B^*(0^+)}$ is taken to be the theoretically predicted value $M_{B^*(0^+)} = 5.68$ GeV [70]. The parameter t_0 is chosen as in Eq. (6.6), and the corresponding value for the $B_s \to K\ell\nu$ process is 16.5 GeV^2. Table IX lists the relevant meson masses used in the z-parametrization fit.

The functional method introduced in Ref. [16] is used to perform the z-parametrization fit, where, following Ref. [16], we take as inputs the results from the chiral-continuum extrapolation and systematic error analysis as presented in Sec. V G.

Our preferred (central) fit has $K = 4$, where K is the number of terms in the expansion in Eq. (6.7). The results of this fit are shown in Table X. These can be used to reconstruct the final form factors as described in Appendix B. We arrive at this preferred fit choice by first simultaneously fitting the form factors f_+ and f_0 with $K = 2$ and without constraining the z-parametrization parameters $b_i^{+,0}$ in Eq. (6.7). The coefficients b_0^+ and b_0^0 are well determined, but the quality of this fit is poor. When increasing K from 2 to 3, the quality of the fit improves, and all the $b_i^{+,0}$ coefficients can be determined well.

TABLE IX. Input meson masses used in the z-parametrization fit.

	M_{B_s}	M_K	M_B	M_π	$M_{B^*}(1^-)$	$M_{B^*}(0^+)$
Value (GeV)	5.36682	0.493677	5.27931	0.1349766	5.32465	5.68

TABLE X. The results of the preferred z-parametrization fit from Eqs. (6.7), (6.6), (6.9), and Table IX with $K = 4$. These values can be used to reconstruct the form factors as explained in Appendix B. The correlation matrix is listed with only four digits after the decimal point. The correlation matrix has one near zero eigenvalue due to the kinematic constraint used. See Appendix B for details.

		Correlation matrix							
	Value	b_0^+	b_1^+	b_2^+	b_3^+	b_0^0	b_1^0	b_2^0	b_3^0
b_0^+	0.3623(0.0178)	1.0000	0.6023	0.0326	−0.1288	0.7122	0.6035	0.5659	0.5516
b_1^+	−0.9559(0.1307)		1.0000	0.4735	0.2677	0.7518	0.9086	0.9009	0.8903
b_2^+	−0.8525(0.4783)			1.0000	0.9187	0.5833	0.7367	0.7340	0.7005
b_3^+	0.2785(0.6892)				1.0000	0.4355	0.5553	0.5633	0.5461
b_0^0	0.1981(0.0101)					1.0000	0.8667	0.7742	0.7337
b_1^0	−0.1661(0.1130)						1.0000	0.9687	0.9359
b_2^0	−0.6430(0.4385)							1.0000	0.9899
b_3^0	−0.3754(0.4535)								1.0000

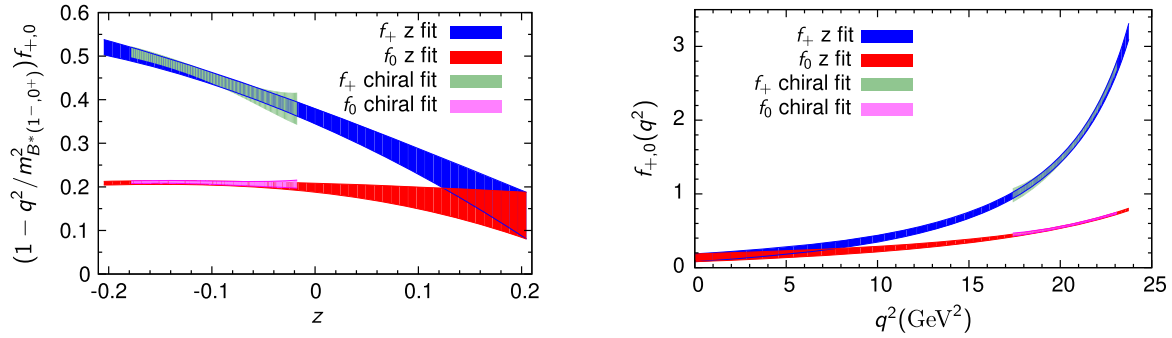

FIG. 12. Preferred $K = 4$ z-parametrization fit results for the form factors f_+ (upper curve) and f_0 (lower curve) as functions of z and q^2. The kinematic constraint Eq. (6.9) is applied. The corresponding bands with larger errors are the results of the chiral-continuum extrapolation, as shown in Sec. IV D. They are used as inputs for the z-parametrization fit. The bands with smaller errors are the resultant z-parametrization fits. The $q^2 = 0$ point corresponds to $z = 0.205$ as shown in Table VIII. The meson poles are listed in Table IX.

The kinematic constraint Eq. (2.2) is satisfied within errors.[4] Enforcing this kinematic constraint, as explained below, further improves the f_+ form-factor fit. The fit parameters also satisfy the unitarity condition [73] and the condition estimated from heavy-quark power counting [79]. Adding the heavy-quark constraint does not affect the fit results. The kinematic constraint is enforced by requiring f_+ and f_0 to be exactly equal at the $q^2 = 0$ point. In practice, we set a prior in the z-parametrization fit

$$f_+(q^2 = 0) - f_0(q^2 = 0) = 0, \tag{6.9}$$

with width $\epsilon = 10^{-10}$. When further increasing the expansion order to $K = 4$, the central value of the form factors at $q^2 = 0$ agrees with the results with $K = 3$, but the error increases. The unitarity and heavy-quark constraints are still satisfied automatically. The results stabilize at $K = 4$ and do not change with $K = 5$. We conclude that the $K = 4$ fit with the kinematic constraint includes the systematic uncertainty due to truncating the z-parametrization series.

The left panel of Fig. 12 shows the preferred $K = 4$ form-factor results, with poles removed, as functions of z. The $q^2 = 0$ point is at the right end of the plot. Note that the shape of the form factors as functions of z is parametrization dependent. For convenience, the right panel of Fig. 12 shows the form factors as functions of q^2. The q^2 dependence of the form factors is parametrization independent and can be used directly to compare with results of other groups.

C. Comparison with existing results

Several other groups have also calculated the same form factors. We note that Refs. [30,31] use the B_sK threshold instead of $B\pi$ in their implementation of the z parametrization. Since the z parameter, by definition [see Eq. (6.3)], depends on the threshold (t_{cut}), we cannot directly compare the z dependence of our form factors with those of Refs. [30,31]. We therefore compare our form factors with those from other lattice QCD calculations only as functions of q^2. This is shown in Fig. 13.

The results of the HPQCD Collaboration [30] are based on $(2 + 1)$-flavor-MILC-asqtad configurations for the sea quarks, and employ the HISQ action for the light valence quarks, and lattice NRQCD for the heavy b quark. The RBC and UKQCD Collaborations [31] use $(2 + 1)$-flavor-domain-wall fermions for the sea quarks and light valence quarks, and a variant [81,82] of the Fermilab action for the heavy b quark. The ALPHA Collaboration [32] uses

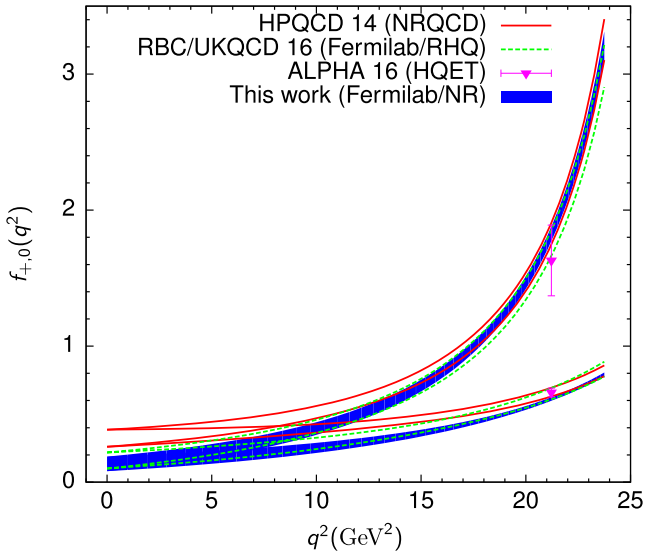

FIG. 13. Theoretical lattice QCD calculations of the $B_s \to K\ell\nu$ form factors from the HPQCD Collaboration [30], the RBC and UKQCD Collaborations [31], the ALPHA Collaboration [32], and the Fermilab Lattice and MILC Collaborations, marked as "This work" in the figure. Different treatments of the bottom quark on the lattice are listed in parenthesis.

[4]Note that the kinematic constraint is automatically satisfied in Eq. (3.5) before taking the extrapolation as is being done in this section. After the extrapolation, this constraint is not guaranteed if not imposed in the fit.

leading-order lattice HQET to get the form factors at one point, $q^2 = 22.12\ \text{GeV}^2$. While our results are consistent with those from Refs. [31,32], they are in tension with HPQCD's results [30]. We note that Ref. [30] employs the so-called modified z expansion, where the chiral-continuum extrapolation is combined with the z expansion into one fit function by modifying the z coefficients with lattice spacing and light-quark-mass dependent terms. This procedure may affect the shape of the form factors. Indeed, in their calculation of the form factors for the $B \to K\ell^+\ell^-$ decay in Ref. [83], the HPQCD Collaboration compared the form factors obtained after the modified z expansion with the results from a two-step method that is very similar to ours, performing first a chiral-continuum extrapolation, and then a z-expansion fit. While they find only small differences between the two sets of form factors, those obtained from their implementation of the two-step method are in better agreement with the results of Ref. [18]. However, unlike the case at hand, the form factors of Ref. [18] are not in significant tension with HPQCD's results of Ref. [83]. We see that the tension between our $B_s \to K\ell\nu$ form factor results and those of Ref. [30] increases with decreasing q^2 to roughly 2.3σ at $q^2 = 0$. The RBC and UKQCD Collaborations [31], on the other hand, adopt the same procedure as we do, namely a chiral-continuum extrapolation at high q^2, followed by a z-expansion extrapolation to $q^2 = 0$.

A comparison of the form factor at $q^2 = 0$ is shown in Fig. 14, where we also include results from calculations using light-cone sum rules [34,35], a relativistic quark model [33], and NLO perturbative QCD [36].

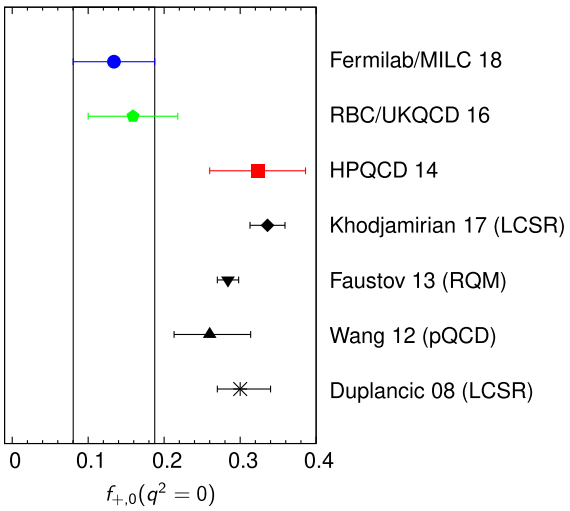

FIG. 14. Comparison of the theoretical calculations of the $B_s \to K\ell\nu$ form factors at $q^2 = 0$. The results shown are from light-cone sum rules (LCSR) [34,35], NLO perturbative QCD (pQCD) [36], relativistic quark model (RQM) [33], and $(2+1)$-flavor lattice QCD (LQCD) from the HPQCD Collaboration [30], the RBC and UKQCD Collaborations [31], and the Fermilab Lattice and MILC Collaborations.

VII. PHENOMENOLOGICAL APPLICATIONS

The angular-dependent differential decay rate for $B_s \to K\ell\nu$ is given in Eq. (2.3). One can construct at most three independent observables from there. In the following, we will consider the differential decay rate $d\Gamma/dq^2$ in Sec. VII A, the forward-backward asymmetry $A_{\text{FB}}^{\ell}(q^2)$ in Sec. VII B, and the lepton polarization asymmetry $A_{\text{pol}}^{\ell}(q^2)$ in Sec. VII C. The latter two quantities are sensitive to the mass of the final-state charged lepton. In Sec. VII D, we also construct the ratios of the scalar and vector form factors between the $B_s \to K\ell\nu$ and $B_s \to D_s\ell\nu$ decays. In Sec. VII E, we briefly compare our results for several quantities with those found in Refs. [30,31].

A. Decay rate

The differential decay rate can be obtained from Eq. (2.3) by integrating over the angle θ_ℓ, which yields

$$\begin{aligned}\frac{d\Gamma}{dq^2} &= \int_{-1}^{1} \frac{d^2\Gamma}{dq^2 d\cos\theta_\ell} d\cos\theta_\ell \\ &= \frac{G_F^2 |V_{ub}|^2}{128\pi^3 M_{B_s}^2}\left(1 - \frac{m_\ell^2}{q^2}\right)^2 |\boldsymbol{p}_K| \\ &\quad \times \left[\frac{16}{3} M_{B_s}^2 |\boldsymbol{p}_K|^2 \left(1 + \frac{m_\ell^2}{2q^2}\right)\left|f_+(q^2)\right|^2 \right. \\ &\quad \left. + \frac{2m_\ell^2}{q^2}(M_{B_s}^2 - M_K^2)^2 |f_0(q^2)|^2\right]. \end{aligned} \tag{7.1}$$

In Fig. 15, we plot the Standard Model predictions of the differential decay rate divided by $|V_{ub}|^2$ over the whole kinematic range of q^2 for $B_s \to K\mu\nu$ and $B_s \to K\tau\nu$.

One can also explore the ratio of the differential decay rates

$$R^{\tau/\mu}(q^2) = \frac{d\Gamma(B_s \to K\tau\nu)/dq^2}{d\Gamma(B_s \to K\mu\nu)/dq^2}. \tag{7.2}$$

Figure 16 shows the prediction for $R^{\tau/\mu}(q^2)$.

The total decay rate is given by

$$\Gamma(B_s \to K\ell\nu) = \int_{m_\ell^2}^{q^2_{\text{max}}} dq^2 \frac{d\Gamma}{dq^2}, \tag{7.3}$$

with $q^2_{\text{max}} = t_- = (M_{B_s} - M_K)^2$, as in Eq. (6.4). The numerical results for $\Gamma/|V_{ub}|^2$ are

$$|V_{ub}|^{-2}\Gamma(B_s \to K\mu\nu) = 4.26(0.92)\ \text{ps}^{-1}, \tag{7.4a}$$

$$|V_{ub}|^{-2}\Gamma(B_s \to K\tau\nu) = 3.27(0.47)\ \text{ps}^{-1}. \tag{7.4b}$$

In Appendix C, we also provide partially integrated differential decay rates in evenly spaced q^2 bins.

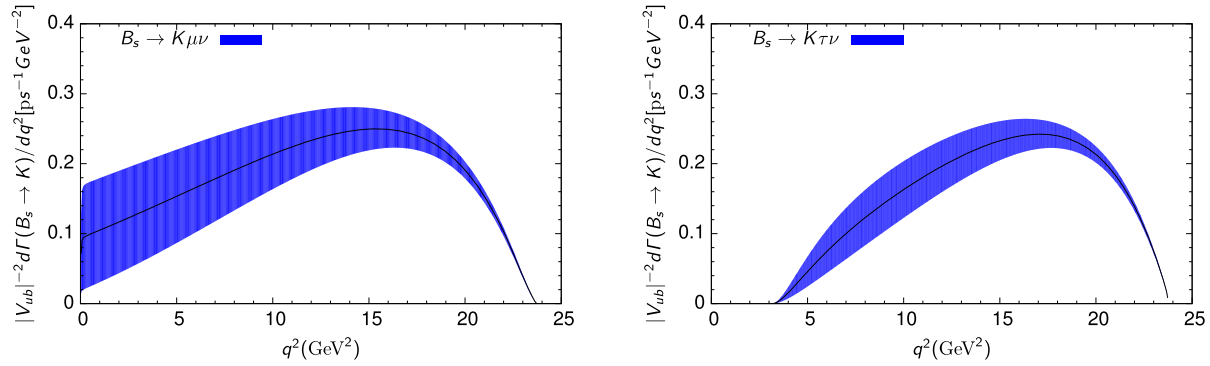

FIG. 15. Standard Model predictions of the differential decay rate divided by $|V_{ub}|^2$ for $B_s \to K\mu\nu$ (left) and $B_s \to K\tau\nu$ (right).

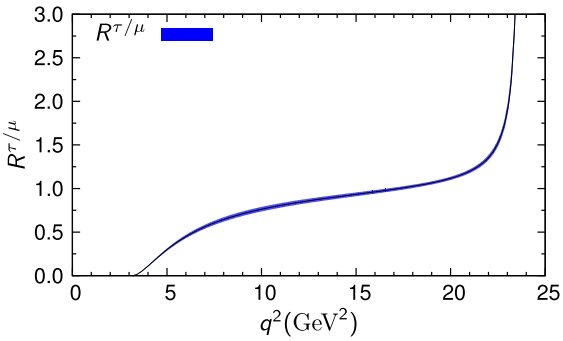

FIG. 16. Standard Model predictions of the ratio of the differential decay rates $R^{\tau/\mu}(q^2)$.

The ratio of the total decay rate is

$$\frac{\Gamma(B_s \to K\tau\nu)}{\Gamma(B_s \to K\mu\nu)} = 0.836(34), \tag{7.5}$$

which takes the correlations between the form factors into account and is more precise than directly using Eq. (7.4).

B. Forward-backward asymmetry

The forward-backward asymmetry, A_{FB}, which depends on the linear $\cos\theta_\ell$ term in Eq. (2.3), is given by

$$\begin{aligned} A_{\mathrm{FB}}^{\ell}(q^2) &= \int_0^1 \frac{d^2\Gamma}{dq^2 d\cos\theta_\ell} d\cos\theta_\ell \\ &\quad - \int_{-1}^0 \frac{d^2\Gamma}{dq^2 d\cos\theta_\ell} d\cos\theta_\ell \\ &= \frac{G_F^2 |V_{ub}|^2}{32\pi^3 M_{B_s}} \left(1 - \frac{m_\ell^2}{q^2}\right)^2 |\boldsymbol{p}_K|^2 \frac{m_\ell^2}{q^2} (M_{B_s}^2 - M_K^2) \\ &\quad \times \mathrm{Re}[f_+(q^2) f_0^*(q^2)]. \end{aligned} \tag{7.6}$$

The Standard Model predictions for the forward-backward asymmetry divided by $|V_{ub}|^2$ are shown in Fig. 17. For the corresponding integrated quantities we find

$$\int_{m_\mu^2}^{q^2_{\mathrm{max}}} dq^2 |V_{ub}|^{-2} A_{\mathrm{FB}}^{\mu}(q^2) = 0.0137(69)\ \mathrm{ps}^{-1}, \tag{7.7a}$$

$$\int_{m_\tau^2}^{q^2_{\mathrm{max}}} dq^2 |V_{ub}|^{-2} A_{\mathrm{FB}}^{\tau}(q^2) = 0.83(14)\ \mathrm{ps}^{-1}. \tag{7.7b}$$

The normalized forward-backward asymmetry is given by

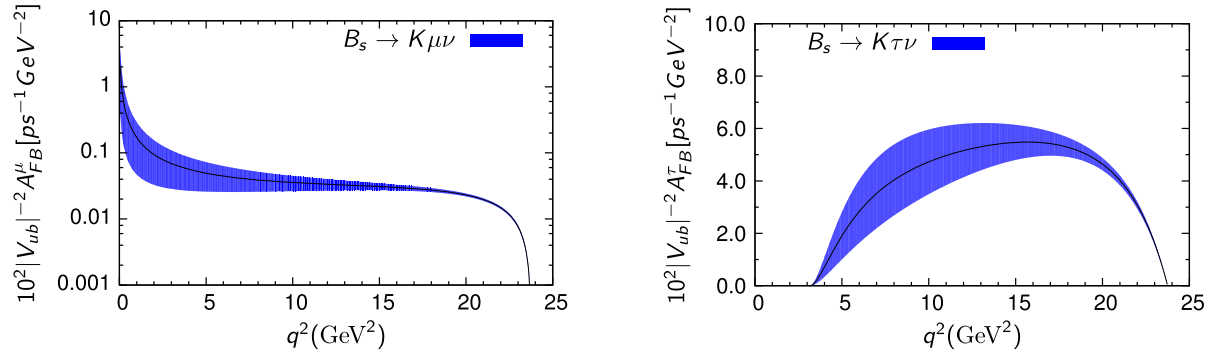

FIG. 17. Standard Model predictions of the forward-backward asymmetry divided by $|V_{ub}|^2$ for $B_s \to K\mu\nu$ (left) and $B_s \to K\tau\nu$ (right).

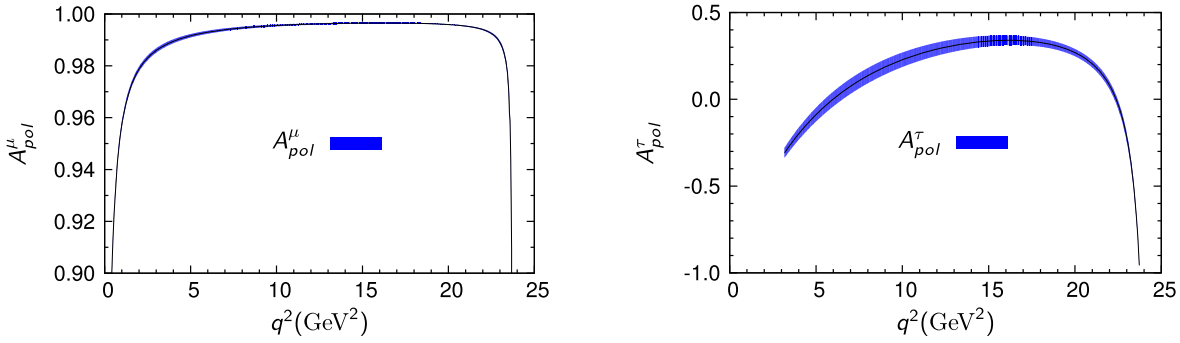

FIG. 18. Standard Model predictions of the normalized lepton polarization asymmetry for $B_s \to K\mu\nu$ (left) and $B_s \to K\tau\nu$ (right).

$$\bar{A}^{\ell}_{\mathrm{FB}} \equiv \frac{\int_{m_\ell^2}^{q^2_{\max}} A^{\ell}_{\mathrm{FB}}(q^2)}{\int_{m_\ell^2}^{q^2_{\max}} d\Gamma/dq^2} \tag{7.8}$$

and the corresponding numerical values are

$$\bar{A}^{\mu}_{\mathrm{FB}} = 0.00321(97), \tag{7.9a}$$

$$\bar{A}^{\tau}_{\mathrm{FB}} = 0.2536(84). \tag{7.9b}$$

C. Lepton polarization asymmetry

The normalized lepton polarization asymmetry is defined as

$$A^{\ell}_{\mathrm{pol}} = \frac{d\Gamma^-/dq^2 - d\Gamma^+/dq^2}{d\Gamma^-/dq^2 + d\Gamma^+/dq^2} \tag{7.10}$$

from the differential decay rates with definite lepton helicity [84]

$$\frac{d\Gamma^-}{dq^2} = \frac{G_F^2|V_{ub}|^2}{24\pi^3}\left(1-\frac{m_\ell^2}{q^2}\right)^2 |\boldsymbol{p}_K|^3 |f_+(q^2)|^2, \tag{7.11a}$$

$$\frac{d\Gamma^+}{dq^2} = \frac{G_F^2|V_{ub}|^2}{24\pi^3}\left(1-\frac{m_\ell^2}{q^2}\right)^2 \frac{m_\ell^2}{q^2}|\boldsymbol{p}_K| \times \left[\frac{3}{8}\frac{(M_{B_s}^2 - M_K^2)^2}{M_{B_s}^2}|f_0(q^2)|^2 + \frac{1}{2}|\boldsymbol{p}_K|^2|f_+(q^2)|^2\right]. \tag{7.11b}$$

Here the superscripts + (−) imply a right- (left-)handed lepton in the final state. The lepton is produced via the $V-A$ current in the Standard Model, and therefore the electron and muon are mainly left-handed polarized. The A^{μ}_{pol} is close to one in the whole q^2 range. Here we provide the normalized lepton polarization asymmetry A^{μ}_{pol} and A^{τ}_{pol} as functions of q^2 in Fig. 18.

D. Ratio of the $B_s \to K\ell\nu$ and $B_s \to D_s\ell\nu$ form factors

We also calculate the ratios of the scalar and vector form factors between the $B_s \to K\ell\nu$ and $B_s \to D_s\ell\nu$ semileptonic decays. The ratios can be used along with future experimental results to determine the ratio of the CKM matrix elements $|V_{ub}/V_{cb}|$.

First, we reconstruct the $B_s \to D_s\ell\nu$ form factors from our previous papers [13,15]. Form factor ratios, $f^{2012}_{+,0}(B_s \to D_s)/f^{2012}_{+,0}(B \to D)$, and the $B \to D\ell\nu$ form factors, $f^{2015}_{+,0}(B \to D)$, are calculated in Refs. [13,15], respectively. They are shown in Fig. 19. The $B_s \to D_s\ell\nu$ form factor can be reconstructed via

$$f^{\mathrm{reco}}_{+,0}(B_s \to D_s) = f^{2015}_{+,0}(B \to D) \times \frac{f^{2012}_{+,0}(B_s \to D_s)}{f^{2012}_{+,0}(B \to D)}. \tag{7.12}$$

With the reconstructed $B_s \to D_s\ell\nu$ form factors $f^{\mathrm{reco}}_{+,0}(B_s \to D_s)$ shown in Fig. 20, we obtain the form-factor ratios, $f_{+,0}(B_s \to K)/f^{\mathrm{reco}}_{+,0}(B_s \to D_s)$, shown in Fig. 21 as functions of q^2 and in Fig. 22 as functions of w. Although the 2012 analysis was carried out on a subset of the ensembles used in the 2015 analysis, we neglect any correlations in the two form factors in Eq. (7.12). Here q^2 is the usual square of the lepton momentum transfer as defined in Eq. (3.2). The recoil parameter w for $B_s \to D_s\ell\nu$ is defined as

$$w = \frac{M_{B_s}^2 + M_{D_s}^2 - q^2}{2M_{B_s}M_{D_s}} \tag{7.13}$$

and the corresponding one for the $B_s \to K\ell\nu$ is defined by replacing M_{D_s} with M_K. The relation between w and q^2 in Eq. (7.13), and the kinematically allowed regions for the two types of processes are shown in Fig. 23. The ratios constructed with different parameters q^2 and w as shown in Figs. 21 and 22 allow us to probe the different $B_s \to K\ell\nu$ form factor regions.

Our reconstructed $B_s \to D_s\ell\nu$ form factor at $q^2 = 0$ is $f^{\mathrm{reco}}_{+,0}(B_s \to D_s, q^2 = 0) = 0.755(65)$, which is larger than that of HPQCD in Ref. [85] $f_0^{(D_s)}(0) = 0.661(42)$. The

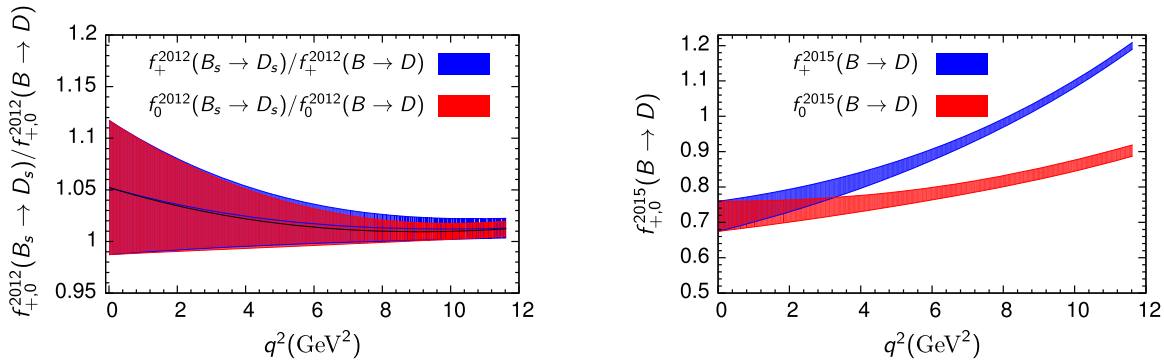

FIG. 19. Form factor ratios, $f_{+,0}^{2012}(B_s \to D_s)/f_{+,0}^{2012}(B \to D)$, calculated by Fermilab Lattice and MILC Collaborations in Ref. [13] in 2012 (left) and $B \to D\ell\nu$ form factors, $f_{+,0}^{2015}(B \to D)$, calculated by the same collaborations in Ref. [15] in 2015 (right). These are the ingredients to reconstruct the $B_s \to D_s\ell\nu$ form factors $f_{+,0}^{\mathrm{reco}}(B_s \to D_s)$.

combination of a smaller $B_s \to K\ell\nu$ form factor, as shown in Fig. 14, and a larger reconstructed $B_s \to D_s\ell\nu$ form factor at $q^2 = 0$ leads to the difference shown in Fig. 21.

E. Comparison with prior results

We very briefly compare our results for a number of quantities calculated in previous subsections with those based on the form factors calculated by the HPQCD Collaboration [30] and by the RBC and UKQCD Collaborations [31].

We have already seen in Figs. 13 and 14 that our form factors agree well with those in Ref. [31] but not with those in Ref. [30]. This is reflected in Table XI where we find quite reasonable agreement with the RBC/UKQCD results

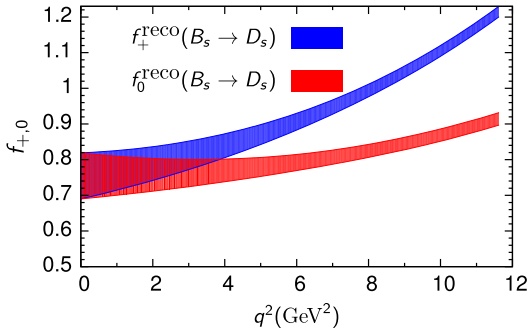

FIG. 20. The reconstructed form factors $f_{+,0}^{\mathrm{reco}}(B_s \to D_s)$ obtained from Eq. (7.12).

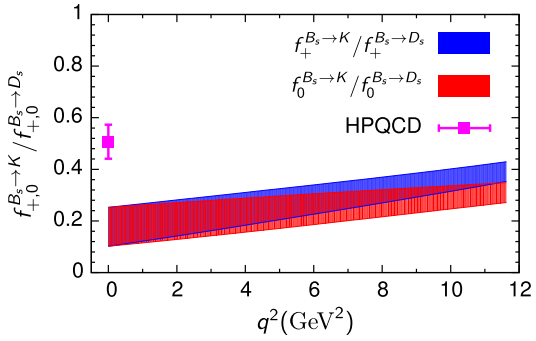

FIG. 21. Form factor ratios, $f_{+,0}(B_s \to K)/f_{+,0}^{\mathrm{reco}}(B_s \to D_s)$, as functions of the momentum transfer q^2. The result provided by HPQCD [85] at $q^2 = 0$ is plotted for comparison.

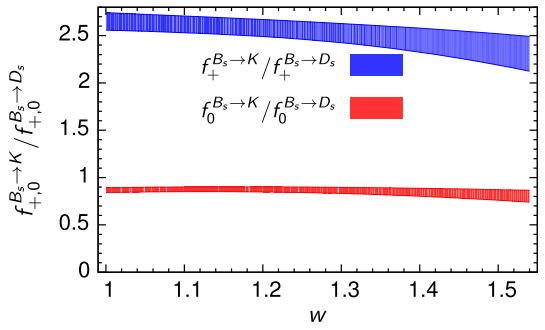

FIG. 22. Form factor ratios, $f_{+,0}(B_s \to K)/f_{+,0}^{\mathrm{reco}}(B_s \to D_s)$, as functions of the recoil parameter w.

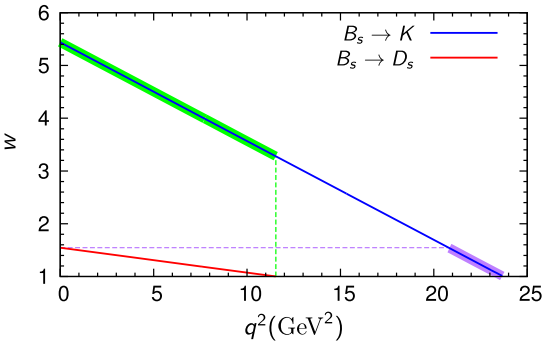

FIG. 23. The kinematically allowed region for $B_s \to K\ell\nu$ (upper solid line) and $B_s \to D_s\ell\nu$ (lower solid line) decays in terms of q^2 and w. The solid lines are the relation between q^2 and w as defined in Eq. (7.13). The green and purple areas are the corresponding $B_s \to K\ell\nu$ regions used to construct the form factor ratios as shown in Fig. 21 and Fig. 22, respectively.

TABLE XI. Comparison of our results with prior calculations. The first column defines the quantity being compared. The second, third, and fourth columns contain our results, those of the RBC and UKQCD Collaborations, [31] and HPQCD Collaboration [30], respectively. The entry in the fourth row of the fourth column corrects a typographical error in Eq. (47) of Ref. [30]. We thank one of the authors for verifying the correction [86].

Quantity (units)	This Work	RBC/UKQCD	HPQCD
$\lvert V_{ub}\rvert^{-2}\Gamma(B_s \to K\mu\nu)(\mathrm{ps}^{-1})$	4.26(0.92)	4.55(1.08)	7.75(1.52)
$\lvert V_{ub}\rvert^{-2}\Gamma(B_s \to K\tau\nu)(\mathrm{ps}^{-1})$	3.27(0.47)	3.52(0.60)	4.92(0.60)
$\Gamma(B_s \to K\tau\nu)/\Gamma(B_s \to K\mu\nu)$	0.836(34)	0.77(12)	0.635(50)
$\int_{m_\mu^2}^{q^2_{\mathrm{max}}} dq^2 \lvert V_{ub}\rvert^{-2} A_{\mathrm{FB}}^{\mu}(q^2)(\mathrm{ps}^{-1})$	0.0137(69)		0.052(17)
$\int_{m_\tau^2}^{q^2_{\mathrm{max}}} dq^2 \lvert V_{ub}\rvert^{-2} A_{\mathrm{FB}}^{\tau}(q^2)(\mathrm{ps}^{-1})$	0.83(14)		1.40(2)
$\bar{A}_{\mathrm{FB}}^{\mu}$	0.00321(97)	0.0039(11)	0.0066(10)
$\bar{A}_{\mathrm{FB}}^{\tau}$	0.2536(84)	0.2650(79)	0.284(17)

but differences between our results and those of HPQCD in the range of 1.6–2.4 standard deviations.

VIII. SUMMARY AND OUTLOOK

Using six strategically selected ensembles of MILC asqtad $2+1$ flavor gauge configurations, we have calculated the form factors $f_+(q^2)$ and $f_0(q^2)$ needed to understand the semileptonic decay $B_s \to K\ell\nu$. We present predictions of the differential decay rate (divided by $|V_{ub}|^2$) for both light (e or μ) or heavy (τ) final-state leptons. Once the experimental data become available, our form factors can be used to determine $|V_{ub}|$, which can then be compared to and, if consistent, combined with the $|V_{ub}|$ determinations from other exclusive decay processes. Hence they may help shed light on the discrepancy with $|V_{ub}|$ from inclusive decays $B \to X_u\ell\nu$ and, perhaps, contribute to evidence for new physics beyond the Standard Model by enabling more stringent tests of the CKM paradigm. Other quantities of phenomenological interest include the forward-backward asymmetry $A_{\mathrm{FB}}^{\ell}(q^2)$ and the lepton polarization asymmetry $A_{\mathrm{pol}}^{\ell}(q^2)$. We also present ratios of the form factors f_+ and f_0 for $B_s \to K\ell\nu$ and $B_s \to D_s\ell\nu$ as functions of both q^2 and w. These may be valuable for determining $|V_{ub}/V_{cb}|$.

Although there are no published results for the decay $B_s \to K\ell\nu$, this process is under investigation by the LHCb experiment, and will be studied by the Belle II Collaboration when they run at the $\Upsilon(5S)$ resonance, which is a copious source of B_s and $\bar{B}_s$ mesons.

On the theoretical side, we have plans to reduce the contributions from the dominant sources of systematic errors in upcoming calculations, which include chiral extrapolation, light and heavy-quark discretization, and renormalization. The gauge ensembles generated by the MILC Collaboration with four flavors of HISQ sea quarks [28,29] are a crucial ingredient in these plans. These ensembles cover a lattice spacing range of approximately 0.15–0.045 fm with physical light quark masses and a dynamical charm quark. The chiral extrapolation becomes a chiral interpolation, and the reduced taste breaking of the HISQ action greatly reduces light quark discretization errors. Using these ensembles, we will be taking two approaches to the b quark. First, we have started a project using Fermilab b quarks (as in this project) and HISQ light valence quarks. Preliminary results were already reported in Refs. [26,87]. As a further small improvement compared to this work, we will include the full correlation matrix between form factors for different processes in our final results. In our second approach, we plan to use the HISQ formalism for the b quark to calculate semileptonic $B_{(s)}$- and D-meson decay form factors again on the HISQ ensembles. Heavy-quark discretization errors are simpler with the HISQ action than with the Fermilab approach, and can be controlled with high precision by including ensembles with very fine lattice spacings in the range of $a \approx 0.03$–0.042 fm. The heavy-HISQ approach also allows us to take advantage of Ward identities when renormalizing the currents. Indeed, our recent work [88] employing the heavy HISQ method for the B- and D-meson decay constants has reached unprecedented precision. We have recently started to generate the needed correlation functions for this project. Finally, we also plan to consider new methods, such as the momentum smearing introduced in Ref. [89], that may allow us to extend the range of recoil momenta accessible to a lattice QCD calculation. In summary, with the improvements outlined above, we expect, in the coming years, to obtain the form factors for $B_s \to K\ell\nu$ (and related decays) with percent level precision, at least in the low recoil region of the phase space.

ACKNOWLEDGMENTS

We thank Jon A. Bailey for participating in the early stage of the project. We thank Chris M. Bouchard for discussions and comments on the form factor comparison section. We thank members of the LHCb Collaboration for discussions and in particular Svende Braun, Marta Calvi, and Mika A. Vesterinen for sharing with us their analysis

status and the preferred q^2 bins. Computations for this work were carried out with resources provided by the USQCD Collaboration, the National Energy Research Scientific Computing Center, the Argonne Leadership Computing Facility, the Blue Waters sustained-petascale computing project, the National Institute for Computational Science, the National Center for Atmospheric Research, the Texas Advanced Computing Center, and Big Red II+ at Indiana University. USQCD resources are acquired and operated thanks to funding from the Office of Science of the U.S. Department of Energy. The National Energy Research Scientific Computing Center is a DOE Office of Science User Facility supported by the Office of Science of the U.S. Department of Energy under Contract No. DE-AC02-05CH11231. An award of computer time was provided by the Innovative and Novel Computational Impact on Theory and Experiment (INCITE) program. This research used resources of the Argonne Leadership Computing Facility, which is a DOE Office of Science User Facility supported under Contract DE-AC02-06CH11357. The Blue Waters sustained-petascale computing project is supported by the National Science Foundation (Awards No. OCI-0725070 and No. ACI-1238993) and the State of Illinois. Blue Waters is a joint effort of the University of Illinois at Urbana-Champaign and its National Center for Supercomputing Applications. This work is also part of the "Lattice QCD on Blue Waters" and "High Energy Physics on Blue Waters" PRAC allocations supported by the National Science Foundation (Grants No. 0832315 and No. 1615006). This work used the Extreme Science and Engineering Discovery Environment (XSEDE), which is supported by National Science Foundation Grant No. ACI-1548562 [90]. Allocations under the Teragrid and XSEDE programs included resources at the National Institute for Computational Sciences (NICS) at the Oak Ridge National Laboratory Computer Center, The Texas Advanced Computing Center and the National Center for Atmospheric Research, all under NSF teragrid allocation TG-MCA93S002. Computer time at the National Center for Atmospheric Research was provided by NSF MRI Grant CNS-0421498, NSF MRI Grant CNS-0420873, NSF MRI Grant CNS-0420985, NSF sponsorship of the National Center for Atmospheric Research, the University of Colorado, and a grant from the IBM Shared University Research (SUR) program. Computing at Indiana University is supported by Lilly Endowment, Inc., through its support for the Indiana University Pervasive Technology Institute. This project was supported in part by the URA Visiting Scholar Award 12-S-15 (Y. L.); by the U.S. Department of Energy under Grants No. DE-FG02-91ER40628 (C. B.), No. DE-FC02-12ER41879 (C. D.), No. DE-FG02-13ER42001 (A. X. K.), No. DE-SC0015655 (A. X. K., Z. G.), No. DE-SC0010120 (S. G.), No. DE-FG02-91ER40661 (S. G.), No. DE-SC0010113 (Y. M.), No. DE-SC0010005 (E. T. N.), No. DE-FG02-13ER41976 (D. T.); by the U.S. National Science Foundation under Grants No. PHY14-14614 and No. PHY17-19626 (C. D.), and No. PHY14-17805 (J. L.); by the MINECO (Spain) under Grants No. FPA2013-47836-C-1-P and No. FPA2016-78220-C3-3-P (E. G.); by the Junta de Andalucía (Spain) under Grant No. FQM-101 (E. G.); by the Fermilab Distinguished Scholars program (A. X. K.); by the German Excellence Initiative and the European Union Seventh Framework Program under Grant Agreement No. 291763 as well as the European Union's Marie Curie COFUND program (A. S. K.). Brookhaven National Laboratory is supported by the United States Department of Energy, Office of Science, Office of High Energy Physics, under Contract No. DE-SC0012704. This document was prepared by the Fermilab Lattice and MILC Collaborations using the resources of the Fermi National Accelerator Laboratory (Fermilab), a U.S. Department of Energy, Office of Science, HEP User Facility. Fermilab is managed by Fermi Research Alliance, LLC (FRA), acting under Contract No. DE-AC02-07CH11359.

APPENDIX A: $B_s \to K\ell\nu$ FORM FACTORS IN SU(2) CHIRAL PERTURBATION THEORY

In this appendix, we derive Eq. (4.6), the SU(2) chiral formula for $B_s \to K\ell\nu$.

We start from the NLO SU(3) HMrSχPT expression for $B_x \to P_{xy}$ semileptonic decay. It is expressed as [69]

$$f_{P,\mathrm{NLO}}^{B_x\to P_{xy}} = f_P^{(0)}[c_P^0(1+\delta f_{P,\mathrm{logs}}) + c_P^x m_x + c_P^y m_y + c_P^{\mathrm{sea}}(m_u+m_d+m_s) + c_P^E E + c_P^{E^2}E^2 + c_P^{a^2}a^2], \tag{A1}$$

where the subscript P stands for $\parallel$ or $\perp$; c_P^i are coefficients and the corresponding rescaled quantities in Eq. (A7) will be determined by the chiral fits; $\delta f_{P,\mathrm{logs}}$ contains the one-loop nonanalytic contributions and wave-function renormalizations; m_x and m_y are the corresponding valence quark masses; m_u, m_d, and m_s are sea quark masses; $E = p\cdot v$ is the P_{xy} meson energy in the B_x meson rest frame; and a is the lattice spacing. The leading order terms for $f_\parallel$ and $f_\perp$ are

$$f_P^{(0)} = \frac{1}{f}\frac{g}{E+\Delta^*_{xy,P}+D_{\mathrm{logs}}}, \tag{A2}$$

where f is the decay constant involved; g is the coupling constant; $\Delta^*_{xy,P}$ is the mass difference between the quantum number $J^P = 0^+$ or 1^- B_y^* meson and the pseudoscalar B_x meson masses at leading order in the chiral expansion, i.e., $\Delta^*_{xy} = B_y^* - B_x$; and D_{logs} is the nonanalytic self-energy contribution. The scalar pole was not included in Ref. [69] as the 0^+ meson is not in leading order HMrSχPT. It is added here phenomenologically as explained in Sec. IV D.

For the $B_s \to K\ell\nu$ analysis considered here, $x = s'$ and $y = u' = d' = u = d$. Here we use primed quantities to denote the valence quarks and the unprimed for the sea quarks.[5] All the data generated for $B_s \to K\ell\nu$ analysis are partially quenched points, i.e., $m'_s \neq m_s$.

In the SU(2) limit, the s-quark mass is treated as infinitely heavy and all the explicit m_s dependent terms are removed from the formula. However, one will still need to keep the mass difference, $m'_s - m_s$, in the leading-order analytic term to take the partial quenching effects into account. In the hard-kaon limit, the kaon with a large energy, E, is integrated out in the nonanalytic chiral expressions. These two limits greatly simplify the expressions of the chiral logs. Following the recipes presented in the Appendix of Ref. [18], we obtain the SU(2) hard-kaon chiral log terms in $f_\parallel$ and $f_\perp$ for the $B_s \to K\ell\nu$ as

$$\delta f^{\mathrm{SU(2)}}_{P,\mathrm{logs}} = \frac{1}{(4\pi f)^2}\left\{\frac{1}{16}\sum_\xi [-I_1(m_{\pi,\xi})] + \frac{1}{4} I_1(m_{\pi,I}) + I_1(m_{\pi,V}) - I_1(m_{\eta,V}) + [V \to A]\right\}, \tag{A3a}$$

$$D^{\mathrm{SU(2)}}_{P,\mathrm{logs}} = 0. \tag{A3b}$$

The summation ξ is over 16 staggered fermion tastes (P, V, T, A, or I); $I_1(m)$ is the chiral logarithm defined as

$$I_1(m) = m^2 \ln\left(\frac{m^2}{\Lambda^2}\right). \tag{A4}$$

Meson masses for the $2+1$ case in the SU(2) limit ($m_u = m_d$ and $m_s \to \infty$) are [18,91]

$$m^2_{\pi,\xi} = m^2_{uu,\xi} = m^2_{dd,\xi}, \tag{A5a}$$

$$m^2_{\eta,V(A)} = m^2_{uu,V(A)} + \frac{1}{2} a^2 \delta'_{V(A)}. \tag{A5b}$$

The $[V \to A]$ in Eq. (A3a) stands for terms with subscripts changed from V to A. The hairpin parameters $\delta'_{V(A)}$ in Eq. (A5b) are listed in Table XII. The $m^2_{ij,\xi}$ are defined later in Eq. (A8).

We can regroup relevant terms in Eq. (A1), drop the m'_s dependent term due to the SU(2) limit, and write the formula as the following

[5]This is different from the convention used in the main text. For example, in Tables I and II the prime quantities denote the sea quarks and the unprimed for the valence ones.

TABLE XII. Fixed parameters used in the chiral-continuum extrapolation fit function. The $r_1^2 a^2 \Delta_\xi$ with $\xi = P, A, T, V, I$, and $r_1^2 a^2 \delta'_{V/A}$ are taste splittings and hairpin parameters.

$\approx a$ (fm)	0.12	0.09	0.06	0
$r_1\mu$	6.831904	6.638563	6.486649	6.015349
$r_1^2 a^2 \Delta_P$	0	0	0	0
$r_1^2 a^2 \Delta_A$	0.22705	0.07469	0.02635	0
$r_1^2 a^2 \Delta_T$	0.36616	0.12378	0.04298	0
$r_1^2 a^2 \Delta_V$	0.48026	0.15932	0.05744	0
$r_1^2 a^2 \Delta_I$	0.60082	0.22065	0.07039	0
$r_1^2 a^2 \delta'_V$	0.0	0.0	0.0	0
$r_1^2 a^2 \delta'_A$	−0.28	−0.09	−0.03	0

$$f_{P,\mathrm{NLO}} = f_P^{(0)}\left[c_P^0(1 + \delta f_{P,\mathrm{logs}}) + \frac{(c_P^u + 2c_P^{\mathrm{sea}})}{3} 3m_u + c_P^{\mathrm{sea}}(m_s - m_{s'}) + c_P^E E + c_P^{E^2} E^2 + c_P^{a^2} a^2\right]. \tag{A6}$$

We can further write all the expansion parameters in terms of dimensionless ones

$$\chi_1 = \frac{3(2\mu m_u)}{8\pi^2 f^2}, \tag{A7a}$$

$$\chi_{\mathrm{h}} = \frac{2\mu(m_s - m'_s)}{8\pi^2 f^2}, \tag{A7b}$$

$$\chi_E = \frac{\sqrt{2}E}{4\pi f}, \tag{A7c}$$

$$\chi_{a^2} = \frac{a^2 \bar{\Delta}}{8\pi^2 f^2}, \tag{A7d}$$

where μ is the leading-order low-energy constant that relates the tree-level mass of a taste-ξ meson composed of quarks of flavor i and j to the corresponding quark masses

$$m^2_{ij,\xi} = \mu(m_i + m_j) + a^2 \Delta_\xi. \tag{A8}$$

Here Δ_ξ is the staggered fermion taste splitting. The numerical values of μ and Δ_ξ are determined by the MILC Collaboration and are shown in Table XII. The average taste splitting in Eq. (A7d) is $\bar{\Delta} = \frac{1}{16}\sum_\xi \Delta_\xi$.

Combining the above information, one arrives at the final NLO form used in the chiral-continuum extrapolation in this work, Eq. (4.6).

APPENDIX B: RECONSTRUCTING THE $B_s \to K\ell\nu$ FORM FACTORS

In this appendix, we document the procedure of reconstructing the form factors from the fitting results obtained in Sec. VI B.

1. Reconstructing the form factors as functions of z

The form factors are parametrized in a BCL [73] form with coefficients $b_i^{+,0}$ as shown in Eq. (6.7). The meson masses used in the z-parametrization fit are listed in Table IX. The fitted coefficients $b_i^{+,0}$ are listed in Table X. To get the form factors as functions of z and reproduce the left panel result of Fig. 12, one should use Eq. (6.7) with $M_{B^*}(1^-)$ and $M_{B^*}(0^+)$ meson mass values in Table IX, and the $b_i^{+,0}$ values and the correlation matrix in Table X.

2. Reconstructing the form factors as functions of q^2

To get the q^2 dependence of the form factors as in the right panel of Fig. 12, one needs the relation between z and q^2. In this paper, the mapping is defined in Eqs. (6.3), (6.1), (6.4), and (6.6). One can then solve Eq. (6.3) to get q^2 in terms of z:

$$q^2(z,t_0) = t_{\rm cut} - \left(\frac{1+z}{1-z}\right)^2 (t_{\rm cut} - t_0). \tag{B1}$$

Once we have the form factors as functions of z from Appendix B 1, we can then use Eq. (B1) to change the variable to get the q^2 dependence.

3. Dealing with the near zero eigenvalue in the covariance matrix

In Table X the fit parameter standard deviations and the correlation matrix are listed. To get the covariance matrix, one only needs to follow the usual procedure to rescale the correlation matrix. The following is the detailed procedure.

Suppose the standard deviation of the fit parameters is

$$\Sigma = [\sigma_1, \sigma_2, \ldots, \sigma_n], \tag{B2}$$

and the matrix D is a diagonal matrix with diagonal elements Σ. The correlation matrix is denoted as R and the covariance matrix is denoted as S. The relations among D, R, and S are

$$S = D \times R \times D, \tag{B3a}$$

$$R = D^{-1} \times S \times D^{-1}. \tag{B3b}$$

Alternatively, one can use the following relation to directly convert the matrix elements

$$S_{ij} = R_{ij}\sigma_i\sigma_j, \tag{B4}$$

where there is no summation over the repeated indices. The covariance matrix, or the inverse of it, is useful when combining form factor results from different sources. It is difficult to calculate the inverse of the covariance matrix from the results listed in Table X. This is because we imposed the kinematical constraint Eq. (6.9) with $\epsilon = 10^{-10}$ in the z-parametrization fit. This results in a near zero eigenvalue in the covariance matrix. The kinematic constraint is equivalent to reducing one parameter in the z parametrization. In principle, one can first reduce one parameter, say b_3^0, in Eq. (6.7), express it in terms of the other $b_i^{+,0}$ parameters, and then perform the z-parametrization fit. This, however, will make the expression Eq. (6.7b) cumbersomely complicated to handle when performing the fit. In practice, we use the expressions Eq. (6.7) and perform the fits as described in Sec. VI B. Whenever one needs to invert the covariance matrix, one simply needs to reduce the size of the matrix by removing one column and one row corresponding to one parameter b_r. The parameter b_r can be any one of the $b_i^{+,0}$ parameters. Without loss of generality, let us pick b_r to be $b_{K-1}^0 = b_3^0$ for our $K = 4$ preferred fit. From Eqs. (6.7) and (6.9), we can get

$$\begin{aligned} b_{K-1}^0(t_0) = \sum_{k=0}^{K-2} \Big[& (b_k^+(t_0) - b_k^0(t_0)) z^{k-K+1} \\ & - (-1)^{k-K} \frac{k}{K} z b_k^+(t_0) \Big] \\ & + b_{K-1}^+(t_0) \left(1 + \frac{K-1}{K} z\right), \end{aligned} \tag{B5}$$

with

$$z \equiv z(q^2 = 0, t_0) = \frac{\sqrt{t_{\rm cut}} - \sqrt{t_{\rm cut} - t_0}}{\sqrt{t_{\rm cut}} + \sqrt{t_{\rm cut} - t_0}}, \tag{B6}$$

as derived from Eq. (6.3).

APPENDIX C: $B_s \to K\ell\nu$ DIFFERENTIAL DECAY RATE BIN TABLES

In this appendix, we present the quantity

$$\frac{1}{|V_{ub}|^2} \int_{q_1^2}^{q_2^2} dq^2 \frac{d\Gamma}{dq^2} \tag{C1}$$

for the $B_s \to K\mu\nu$ and $B_s \to K\tau\nu$ decays, in bins of q^2, in Tables XIII and XIV. Since we also include the correlations between q^2 bins in these tables, the results therein can be combined with the corresponding experimental measurements to determine $|V_{ub}|$.

TABLE XIII. The binned differential decay rates, defined in Eq. (C1), and their correlations for $B_s \to K\mu\nu$ in twelve evenly spaced q^2 bins.

		Correlation matrix											
$\Delta q^2(\mathrm{GeV}^2)$	Value	0–2	2–4	4–6	6–8	8–10	10–12	12–14	14–16	16–18	18–20	20–22	22–24
0–2	0.20707(0.14609)	1.0000	0.9981	0.9911	0.9766	0.9510	0.9096	0.8459	0.7520	0.6171	0.4280	0.1869	−0.0067
2–4	0.25741(0.14256)		1.0000	0.9974	0.9880	0.9681	0.9332	0.8765	0.7893	0.6599	0.4715	0.2200	0.0060
4–6	0.30678(0.13329)			1.0000	0.9965	0.9836	0.9564	0.9082	0.8297	0.7076	0.5217	0.2600	0.0237
6–8	0.35666(0.12140)				1.0000	0.9952	0.9773	0.9396	0.8720	0.7599	0.5790	0.3085	0.0484
8–10	0.40477(0.10755)					1.0000	0.9933	0.9683	0.9147	0.8160	0.6440	0.3674	0.0830
10–12	0.44785(0.09239)						1.0000	0.9906	0.9545	0.8742	0.7169	0.4396	0.1323
12–14	0.48121(0.07653)							1.0000	0.9862	0.9306	0.7967	0.5285	0.2033
14–16	0.49783(0.06056)								1.0000	0.9778	0.8804	0.6382	0.3069
16–18	0.48688(0.04502)									1.0000	0.9585	0.7714	0.4589
18–20	0.43098(0.03061)										1.0000	0.9170	0.6736
20–22	0.30246(0.01787)											1.0000	0.9090
22–24	0.08453(0.00502)												1.0000

TABLE XIV. The binned differential decay rates, defined in Eq. (C1), and their correlations for $B_s \to K\tau\nu$ in eleven evenly spaced q^2 bins.

		Correlation matrix										
$\Delta q^2(\mathrm{GeV}^2)$	Value	2–4	4–6	6–8	8–10	10–12	12–14	14–16	16–18	18–20	20–22	22–24
2–4	0.00500(0.00269)	1.0000	0.9993	0.9953	0.9851	0.9648	0.9281	0.8640	0.7522	0.5581	0.2683	0.0393
4–6	0.09085(0.04127)		1.0000	0.9982	0.9909	0.9740	0.9414	0.8819	0.7747	0.5837	0.2913	0.0544
6–8	0.19913(0.07215)			1.0000	0.9971	0.9857	0.9595	0.9074	0.8081	0.6229	0.3277	0.0797
8–10	0.28718(0.08104)				1.0000	0.9956	0.9779	0.9359	0.8477	0.6718	0.3761	0.1156
10–12	0.36067(0.07799)					1.0000	0.9931	0.9643	0.8915	0.7302	0.4384	0.1660
12–14	0.42097(0.06852)						1.0000	0.9885	0.9370	0.7986	0.5192	0.2379
14–16	0.46455(0.05576)							1.0000	0.9786	0.8763	0.6252	0.3429
16–18	0.48267(0.04190)								1.0000	0.9554	0.7621	0.4978
18–20	0.45879(0.02887)									1.0000	0.9162	0.7121
20–22	0.36241(0.01781)										1.0000	0.9256
22–24	0.14148(0.00609)											1.0000

[1] P. del Amo Sanchez *et al.* (*BABAR* Collaboration), Phys. Rev. D **83**, 032007 (2011).
[2] J. P. Lees *et al.* (*BABAR* Collaboration), Phys. Rev. D **86**, 092004 (2012).
[3] H. Ha *et al.* (Belle Collaboration), Phys. Rev. D **83**, 071101 (2011).
[4] A. Sibidanov *et al.* (Belle Collaboration), Phys. Rev. D **88**, 032005 (2013).
[5] M. Tanabashi *et al.* (Particle Data Group), Phys. Rev. D **98**, 030001 (2018).
[6] G. Ciezarek, A. Lupato, M. Rotondo, and M. Vesterinen, J. High Energy Phys. 02 (2017) 021.
[7] P. Urquijo, Nucl. Part. Phys. Proc. **263–264**, 15 (2015).
[8] A. Bazavov *et al.* (Fermilab Lattice and MILC Collaborations), Phys. Rev. D **87**, 073012 (2013).
[9] C. Aubin *et al.* (Fermilab Lattice, MILC, and HPQCD Collaborations), Phys. Rev. Lett. **94**, 011601 (2005).
[10] C. Bernard *et al.* (Fermilab Lattice and MILC Collaborations), Phys. Rev. D **79**, 014506 (2009).
[11] J. A. Bailey *et al.* (Fermilab Lattice and MILC Collaborations), Phys. Rev. D **79**, 054507 (2009).
[12] J. A. Bailey *et al.* (Fermilab Lattice and MILC Collaborations), Phys. Rev. Lett. **109**, 071802 (2012).
[13] J. A. Bailey *et al.* (Fermilab Lattice and MILC Collaborations), Phys. Rev. D **85**, 114502 (2012); **86**, 039904 (2012).
[14] J. A. Bailey *et al.* (Fermilab Lattice and MILC Collaborations), Phys. Rev. D **89**, 114504 (2014).
[15] J. A. Bailey *et al.* (Fermilab Lattice and MILC Collaborations), Phys. Rev. D **92**, 034506 (2015).

[16] J. A. Bailey *et al.* (Fermilab Lattice and MILC Collaborations), Phys. Rev. D **92**, 014024 (2015).
[17] J. A. Bailey *et al.* (Fermilab Lattice and MILC Collaborations), Phys. Rev. Lett. **115**, 152002 (2015).
[18] J. A. Bailey *et al.* (Fermilab Lattice and MILC Collaborations), Phys. Rev. D **93**, 025026 (2016).
[19] D. Du, A. X. El-Khadra, S. Gottlieb, A. S. Kronfeld, J. Laiho, E. Lunghi, R. S. Van de Water, and R. Zhou (Fermilab Lattice Collaboration), Phys. Rev. D **93**, 034005 (2016).
[20] C. W. Bernard, T. Burch, K. Orginos, D. Toussaint, T. A. DeGrand, C. E. DeTar, S. Datta, S. A. Gottlieb, U. M. Heller, and R. Sugar (MILC Collaboration), Phys. Rev. D **64**, 054506 (2001).
[21] C. Aubin, C. Bernard, C. DeTar, J. Osborn, S. Gottlieb, E. B. Gregory, D. Toussaint, U. M. Heller, J. E. Hetrick, and R. Sugar (MILC Collaboration), Phys. Rev. D **70**, 094505 (2004).
[22] A. Bazavov *et al.*, Rev. Mod. Phys. **82**, 1349 (2010).
[23] A. Bazavov *et al.* (Fermilab Lattice and MILC Collaborations), Phys. Rev. Lett. **112**, 112001 (2014).
[24] E. Gámiz *et al.* (Fermilab Lattice and MILC Collaborations), Proc. Sci., LATTICE2016 (**2016**) 286.
[25] T. Primer *et al.* (Fermilab Lattice and MILC Collaborations), Proc. Sci., LATTICE2016 (**2017**) 305.
[26] Z. Gelzer *et al.* (Fermilab Lattice and MILC Collaborations), EPJ Web Conf. **175**, 13024 (2018).
[27] A. Bazavov *et al.* (Fermilab Lattice and MILC Collaborations), arXiv:1809.02827.
[28] A. Bazavov *et al.* (MILC Collaboration), Phys. Rev. D **82**, 074501 (2010).
[29] A. Bazavov *et al.* (MILC Collaboration), Phys. Rev. D **87**, 054505 (2013).
[30] C. M. Bouchard, G. P. Lepage, C. Monahan, H. Na, and J. Shigemitsu (HPQCD Collaboration), Phys. Rev. D **90**, 054506 (2014).
[31] J. M. Flynn, T. Izubuchi, T. Kawanai, C. Lehner, A. Soni, R. S. Van de Water, and O. Witzel (RBC/UKQCD Collaboration), Phys. Rev. D **91**, 074510 (2015).
[32] F. Bahr, D. Banerjee, F. Bernardoni, A. Joseph, M. Koren, H. Simma, and R. Sommer (ALPHA Collaboration), Phys. Lett. B **757**, 473 (2016).
[33] R. N. Faustov and V. O. Galkin, Phys. Rev. D **87**, 094028 (2013).
[34] G. Duplancic and B. Melic, Phys. Rev. D **78**, 054015 (2008).
[35] A. Khodjamirian and A. V. Rusov, J. High Energy Phys. 08 (2017) 112.
[36] W.-F. Wang and Z.-J. Xiao, Phys. Rev. D **86**, 114025 (2012).
[37] Y. Liu *et al.* (Fermilab Lattice and MILC Collaborations), Proc. Sci., LATTICE2013 (**2014**) 386.
[38] Y. Liu *et al.* (Fermilab Lattice and MILC Collaborations), EPJ Web Conf. **175**, 13008 (2018).
[39] M. Lüscher and P. Weisz, Commun. Math. Phys. **97**, 59 (1985); **98**, 433 (1985).
[40] T. Blum, C. E. DeTar, S. A. Gottlieb, K. Rummukainen, U. M. Heller, J. E. Hetrick, D. Toussaint, R. L. Sugar, and M. Wingate (MILC Collaboration), Phys. Rev. D **55**, R1133 (1997).
[41] G. P. Lepage, Nucl. Phys. B, Proc. Suppl. **60A**, 267 (1998).
[42] J. F. Lagaë and D. K. Sinclair, Phys. Rev. D **59**, 014511 (1998).
[43] G. P. Lepage, Phys. Rev. D **59**, 074502 (1999).
[44] K. Orginos and D. Toussaint (MILC Collaboration), Phys. Rev. D **59**, 014501 (1998).
[45] K. Orginos, D. Toussaint, and R. L. Sugar (MILC Collaboration), Phys. Rev. D **60**, 054503 (1999).
[46] C. W. Bernard, T. Burch, T. A. DeGrand, C. E. DeTar, S. A. Gottlieb, U. M. Heller, J. E. Hetrick, K. Orginos, B. Sugar, and D. Toussaint (MILC Collaboration), Phys. Rev. D **61**, 111502 (2000).
[47] B. Sheikholeslami and R. Wohlert, Nucl. Phys. **B259**, 572 (1985).
[48] A. X. El-Khadra, A. S. Kronfeld, and P. B. Mackenzie, Phys. Rev. D **55**, 3933 (1997).
[49] MILC Collaboration, asqtad ensemble 04a, https://doi.org/10.15484/milc.asqtad.en04a/1178155 (2015).
[50] MILC Collaboration, asqtad ensemble 15a, https://doi.org/10.15484/milc.asqtad.en15a/1178095 (2015).
[51] MILC Collaboration, asqtad ensemble 15b, https://doi.org/10.15484/milc.asqtad.en15b/1178096 (2015).
[52] MILC Collaboration, asqtad ensemble 15c, https://doi.org/10.15484/milc.asqtad.en15c/1178097 (2015).
[53] MILC Collaboration, asqtad ensemble 14a, https://doi.org/10.15484/milc.asqtad.en14a/1178094 (2015).
[54] MILC Collaboration, asqtad ensemble 13a, https://doi.org/10.15484/milc.asqtad.en13a/1178092 (2015).
[55] MILC Collaboration, asqtad ensemble 13b, https://doi.org/10.15484/milc.asqtad.en13b/1178093 (2015).
[56] MILC Collaboration, asqtad ensemble 12a, https://doi.org/10.15484/milc.asqtad.en12a/1178091 (2015).
[57] MILC Collaboration, asqtad ensemble 18a, https://doi.org/10.15484/milc.asqtad.en18a/1178033 (2015).
[58] MILC Collaboration, asqtad ensemble 18b, https://doi.org/10.15484/milc.asqtad.en18b/1178034 (2015).
[59] R. Sommer, Nucl. Phys. **B411**, 839 (1994).
[60] C. W. Bernard, T. Burch, K. Orginos, D. Toussaint, T. A. DeGrand, C. E. DeTar, S. A. Gottlieb, U. M. Heller, J. E. Hetrick, and B. Sugar, Phys. Rev. D **62**, 034503 (2000).
[61] A. Bazavov *et al.* (Fermilab Lattice and MILC Collaborations), Phys. Rev. D **85**, 114506 (2012).
[62] M. Wingate, J. Shigemitsu, C. T. H. Davies, G. P. Lepage, and H. D. Trottier, Phys. Rev. D **67**, 054505 (2003).
[63] N. Kawamoto and J. Smit, Nucl. Phys. **B192**, 100 (1981).
[64] J. Harada, S. Hashimoto, K.-I. Ishikawa, A. S. Kronfeld, T. Onogi, and N. Yamada, Phys. Rev. D **65**, 094513 (2002); **71**, 019903 (2005).
[65] A. X. El-Khadra, A. S. Kronfeld, P. B. Mackenzie, S. M. Ryan, and J. N. Simone, Phys. Rev. D **64**, 014502 (2001).
[66] A. Bazavov *et al.* (Fermilab Lattice and MILC Collaborations), Phys. Rev. D **93**, 113016 (2016).
[67] C. Patrignani *et al.* (Particle Data Group), Chin. Phys. C **40**, 100001 (2016).
[68] C. Aubin and C. Bernard, Phys. Rev. D **73**, 014515 (2006).
[69] C. Aubin and C. Bernard, Phys. Rev. D **76**, 014002 (2007).
[70] E. B. Gregory *et al.* (HPQCD Collaboration), Phys. Rev. D **83**, 014506 (2011).
[71] B. Chakraborty, C. Davies, G. Donald, R. Dowdall, J. Koponen, and G. P. Lepage (HPQCD Collaboration), Proc. Sci., LATTICE2013 (**2014**) 309.

[72] A. X. El-Khadra, E. Gamiz, A. S. Kronfeld, and M. A. Nobes, Proc. Sci., LATTICE2007 (**2007**) 242.
[73] C. Bourrely, I. Caprini, and L. Lellouch, Phys. Rev. D **79**, 013008 (2009); **82**, 099902(E) (2010).
[74] R. Eden, P. Landshoff, D. Olive, and J. Polkinghorne, *The Analytic S-Matrix* (Cambridge University Press, Cambridge, England, 1966).
[75] G. P. Lepage and S. J. Brodsky, Phys. Rev. D **22**, 2157 (1980).
[76] R. Akhoury, G. F. Sterman, and Y. P. Yao, Phys. Rev. D **50**, 358 (1994).
[77] N. Meiman, Zh. Eksp. Teor. Fiz. **44**, 1228 (1963) [Sov. Phys. JETP **17**, 830 (1963)].
[78] S. Okubo, Phys. Rev. D **3**, 2807 (1971).
[79] T. Becher and R. J. Hill, Phys. Lett. B **633**, 61 (2006).
[80] C. G. Boyd, B. Grinstein, and R. F. Lebed, Phys. Rev. Lett. **74**, 4603 (1995).
[81] H.-W. Lin and N. Christ, Phys. Rev. D **76**, 074506 (2007).
[82] N. H. Christ, M. Li, and H.-W. Lin, Phys. Rev. D **76**, 074505 (2007).
[83] C. Bouchard, G. P. Lepage, C. Monahan, H. Na, and J. Shigemitsu (HPQCD Collaboration), Phys. Rev. D **88**, 054509 (2013); **88**, 079901(E) (2013).
[84] U.-G. Meiß ner and W. Wang, J. High Energy Phys. 01 (2014) 107.
[85] C. J. Monahan, C. M. Bouchard, G. P. Lepage, H. Na, and J. Shigemitsu, Phys. Rev. D **98**, 114509 (2018).
[86] C. M. Bouchard (private communication).
[87] Z. Gelzer *et al.* (Fermilab Lattice and MILC Collaborations), Proc. Sci., LATTICE2018 (**2018**) 289.
[88] A. Bazavov *et al.*, Phys. Rev. D **98**, 074512 (2018).
[89] G. S. Bali, B. Lang, B. U. Musch, and A. Schäfer, Phys. Rev. D **93**, 094515 (2016).
[90] J. Towns, T. Cockerill, M. Dahan, I. Foster, K. Gaither, A. Grimshaw, V. Hazlewood, S. Lathrop, D. Lifka, G. D. Peterson, R. Roskies, J. R. Scott, and N. Wilkins-Diehr, Comput. Sci. Eng. **16**, 62 (2014).
[91] C. Aubin and C. Bernard (MILC Collaboration), Phys. Rev. D **68**, 034014 (2003).